ELSEVIER

Microstructural Evolution and Age Hardening in Aluminium Alloys: Atom Probe Field-Ion Microscopy and Transmission Electron Microscopy Studies

S. P. Ringer* and K. Hono†

**Department of Materials Engineering, Monash University, Clayton, Victoria, 3168, Australia; and †National Research Institute for Metals, Tsukuba 305-0047, Japan*

This paper examines the microstructural evolution in selected aluminium alloys based on commercial age hardenable 2000, 6000, and 7000 series alloys. Atom probe field-ion microscopy and transmission electron microscopy have been used to examine the effects of microalloying and the origins of hardening. The combined application of these techniques is particularly important in the study of nanoscale precipitation processes. It is shown that the nature and kinetics of the precipitation process depend on the solute–solute interactions that produce solute clusters. The solute clusters precede the formation of GP zones or precipitation, and have a defining role on the nature and kinetics of the subsequent precipitation processes. Moreover, interactions between solute clustering and dislocations can have a significant hardening effect, the origins of which seem to be distinctly different from the conventional notion of precipitation hardening.

INTRODUCTION

Most wrought aluminium alloys are strengthened by age hardening. The precipitation processes from which this hardening is derived are well known to be sensitive to the presence of selected trace element additions or microalloying, which can change the process and/or kinetics of precipitation in many age hardenable alloys [1, 2]. Precipitation in commercial aluminium alloys usually starts from the formation of GP zones, which may be regarded as fully coherent metastable precipitates. Subsequent evolution of the microstructure involves the replacement of the GP zones with more stable phases. This occurs primarily because GP zones are isomorphous with the matrix and, therefore, have a lower interfacial energy than intermediate or equilibrium precipitate phases that possess a distinct crystal structure. As a result, the nucleation barrier for GP zones is significantly smaller. The typical size of GP zones is in the order of tens of nanometers, and the chemical composition of these precipitates is not easily measured, even with a state-of-the-art analytical electron microscope. Furthermore, many experimental results suggest that solute clustering occurs prior to the precipitation of GP zones, and this modifies both the nature and kinetics of the precipitation process. Although GP zones are readily observed by modern TEM, clear observation of solute clusters is not possible, even with a high-resolution transmission electron microscope (HRTEM). The atom probe can detect single atoms, and thus, it is possible to clearly detect the clustering of solute, which appears to be the earliest stage of age hardening. Thus, the use of the atom probe technique for studies on precipitation processes can shed light on many of the re-

MATERIALS CHARACTERIZATION 44:101–131 (2000)

655 Avenue of the Americas, New York, NY 10010

1044-5803/00/$–see front matter
PII S1044-5803(99)00051-0

maining problems in the physical metallurgy of age-hardenable aluminium alloys. This is also of current technological interest, given that variations in the heat treatment, strain conditions prior to aging, and alloy composition induce significant changes in microstructure, and there remains considerable potential for the design of high-strength aluminium alloys. Recent technological impetus for exploring the alloy design and development has mainly come from the aerospace and automobile industries [1].

The purpose of this review is to examine the microstructural mechanisms underlying the aging processes in a selection of wrought heat-treatable alloys. A feature of this review is the application of atom probe field-ion microscopy (APFIM) and transmission electron microscopy (TEM) in providing direct observations of the evolution of microstructure and an insight to the age-hardening processes.

EXPERIMENTAL

Most of the studies reported here were performed on scientific alloys. Ingots were conventionally cast into book molds, homogenized at 525°C for ~72 h, and scalped (5mm from each face). Samples (~5 × ~10 × ~10mm) were machined for hardness testing, while some material was cold rolled to sheet for TEM studies. Samples for APFIM xwere spark machined from the bulk to 0.3 × 0.3 × 10mm or obtained from material drawn to wire. Solution treatment was carried out in either salt or Ar atmospheres, followed by cold-water quenching. Elevated temperature aging was performed in silicone oil baths, and hardness monitored using a standard Vickers hardness indentor under a load of 5kg. Samples for APFIM and TEM were prepared using standard electropolishing techniques [3, 4].

Details describing the APFIM instrumentation are provided in references [5–7]. An important feature of the APFIM instrumentation used in these studies is the ability to cool specimens to ~20K, which allows stable field ion microscopy (FIM) of aluminium alloys. Until recently, FIM and atom-probe analyses of aluminium alloys was uncommon, while other major industrial metallic materials such as steels were extensively studied. This was mainly because of the low evaporation field of Al, which makes the observation of FIM images difficult. By lowering the specimen temperature to ~20K, the evaporation field of Al becomes as high as the ionization fields of Ne and He, allowing stable FIM observations using these imaging gases [3]. The first FIM image of an Al alloy was obtained by Boyes et al. [8], using a cold finger cooled down by liquid He. Later, using a dedicated FIM, good-quality FIM images of Al–Cu alloys were obtained by Abe et al. [9], Wada et al. [10], and Hono et al. [11]. In an atom probe, however, a specimen-tilting mechanism must be incorporated in the FIM, and achieving ~20K is not trivial. In all of the studies reviewed here, FIM images were obtained using either Ne gas at ~35K, or He gas at ~25K. The one-dimensional (1D) atom probes employed either Poschenrieder or reflectron energy compensating lenses. The 1DAP analyses were typically performed with ~0.5nm spatial resolution in the lateral direction and atomic layer resolution in the depth direction. A three-dimensional atom probe (3DAP), equipped with CAMECA's tomographic atom probe [7] was also employed. Both 1D and 3DAP analyses were performed at a specimen temperature of ~20–30K in ultrahigh vacuum (10^{-11} Torr) using a pulse fraction of either 15 or 20% and a pulse rate of 100 or 600Hz. Visualization and analysis of the 3DAP data was carried out using the Kindbrisk SDV 3DAP data analysis software running on the Advanced Visualization System (AVS).

The present work also contains results from conventional transmission electron microscopy (CTEM) and high-resolution transmission electron microscopy (HRTEM). A suite of microscopes were used including a Philips CM12 (120kV), Philips CM20 (200kV), JEOL 2000 EX (200kV), JEOL 4000

EX (400kV), and a JEOL ARM operating at 600kV.

Al-Cu BASED ALLOYS

The most widely studied age-hardening alloy system is Al–Cu, and several commercial alloys based on this system remain in use in the 2xxx alloy series. Although the alloy is composed of only two elements, the microstructural evolution is complex, and the precipitation sequence varies depending on the degree of supersaturation and the aging temperature. Figure 1 shows the Al-rich corner of the equilibrium Al–Cu phase diagram, and includes the metastable solvus boundaries for GP zones, θ″ and θ′. Over many studies [9–29], it has been proposed that the decomposition sequence in this system contains one or more of the following processes:

Supersaturated Solid Solution (SSSS) →
GP zones → θ" → θ' → θ

The complete precipitation sequence can only occur when the alloy is aged at temperatures below the GP zone solvus (Fig. 1). Various steps in this process may be suppressed by aging at temperatures close to or above the intermediate solvus temperatures. Figure 2 shows a hardness–time plot for Al–1.7Cu-aged at 130 and 190°C, which represents temperatures below and above the GP zone solvus temperature, respectively. The first stage of hardening at 130°C is attributed to the formation of GP zones. After reaching a critical diameter of between 5 and 10nm, an incubation period commences, during which the zone size and the hardness remain constant [15–17]. Further aging results in a second rise in hardness, attributed to θ″ precipitation. The formation of θ″ is also followed by a shorter incubation period and the subsequent formation of the metastable θ′ phase. Prolonged aging results in the formation of the equilibrium θ phase. Each precipitation stage does not necessarily correspond to the stages observed in the hardness curve, and more than two phases can coexist at a given stage of the aging process. The mechanism of the transformation sequence from one phase to another usually involves heterogeneous nucleation at the sites of earlier products, resulting in fine and uniform precipitate dispersions. However, under a suitable degree of supersaturation, the products in the above evolutionary sequence nucleate directly into the matrix [17]. This

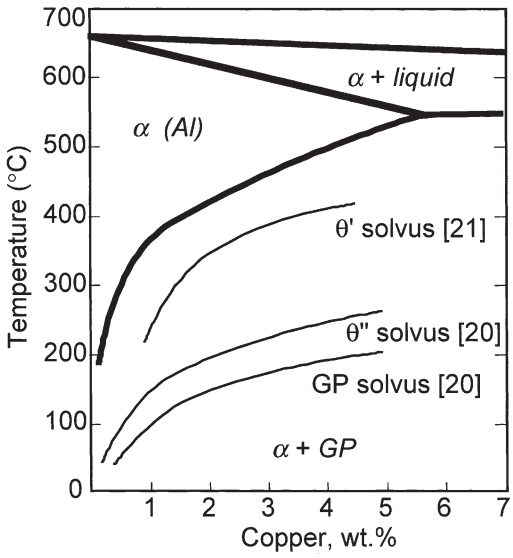

FIG. 1. Al-rich corner of the Al–Cu phase diagram showing the metastable solvus boundaries for GP zones, θ″ and θ′, together with the equilibrium solvus line for the θ phase. After Beton and Rollason [20] and Murray [21].

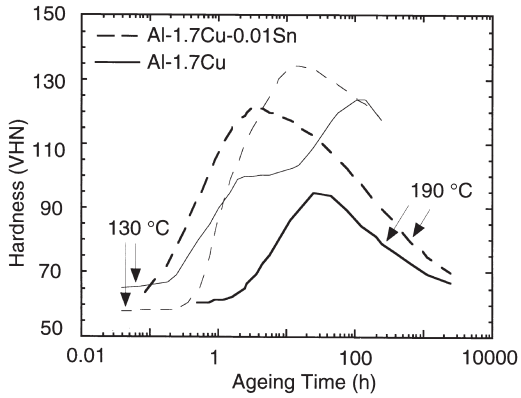

FIG. 2. Hardness–time plot for Al–1.7Cu aged at 130 and 190°C, showing the effect of a 0.01 Sn addition. After Hardy [16].

is precisely what occurs when the alloy is aged at 190°C (Fig. 2). Single-stage hardening occurs here because the temperature is above the solvus for the GP zones and θ″ nucleates directly. However, the smaller driving force for precipitation, together with the lower volume fraction of θ″ at 190°C (Fig. 1), results in a coarser dispersion and a lower peak hardness. The kinetics of the aging process are faster at this temperature due to the higher solute diffusivity, and this produces a shorter time to peak hardness than that at 130°C. The nucleation of θ′ at θ″ sites is similarly accelerated at 190°C.

To understand the mechanism of the increase in hardness that accompanies aging, it is useful to examine the individual stages of the microstructural evolution described above. By the early 1960s, X-ray diffraction and resistivity measurements suggested that solute atoms may spontaneously cluster in certain Al alloys after quenching to temperatures below the metastable GP zone solvus line [23–25, 30]. The formation of these clusters precedes the formation of GP zones. In the Al–Cu system, Rioja and Laughlin [12] interpreted the observation of diffuse satellites in selected area electron diffraction (SAED) patterns, as evidence for spinodal decomposition. Moreover, Matsubara and Cohen [25] have reported absolute X-ray intensity measurements that indicate that the Cu atoms are in a nonrandom distribution even at the solution treatment temperature and in the as-quenched (AQ) state. Despite the high electron scattering amplitude of Cu, Nicholson et al. [14] have pointed out that these clusters are difficult to observe by TEM, due to the need for very thin foils so as to improve the average scattering from the clusters. These clusters have been observed in FIM studies of AQ Al–1.7Cu alloys, and the concentration fluctuations that they cause are readily detected in corresponding 1DAP analyses [11].

Following the X-ray diffraction (XRD) work by Guinier [26] and Preston [27], there have been numerous studies of GP zones, involving XRD [17], small-angle X-ray scattering [22], resistivity [23, 24], CTEM [14], HRTEM [19, 28, 29], and APFIM [11]. There is now general agreement that GP zones are single-atom layers of Cu on $\{001\}_\alpha$ planes. However, multilayer GP zones have also been observed [11]. Figure 3(a) provides a series of Ne FIM images from a field-evaporation sequence of four $(022)_\alpha$ planes. The sections of the zone observed in the $[100]_\alpha$ direction are always observed as a two-layer atomic row, providing direct evidence for a two-layer thickness of Cu atoms. Models for the single-layer and multilayer GP zones are provided in Fig. 3(b–c). The single- and multilayer models for GP zones are distinct from that of the θ″ phase, which is considered as two layers of Cu separated by three $\{001\}_\alpha$ layers of Al [Fig. 3(d)] [11, 17]. While the disc or planer-shaped GP zones exhibit a rod-like shape effect normal to their $\{100\}_\alpha$ habit planes, giving rise to continuous streaking in $<010>_\alpha$ directions in SAED patterns, the θ″ phase is distinguished in $<100>_\alpha$ SAED patterns by the occurrence of intensity maxima at the $\{010\}_\alpha$ positions, elongated along the $<010>_\alpha$ directions [18, 19]. Atom-probe studies on GP zones and the θ″ phase are consistent with the structural features described above. The results of 1DAP suggest that the Cu composition of GP zones is approximately 33 atomic percent (at. %), which is the same as that of the equilibrium phase [11]. In the case of the θ″ phase, two peaks in the Cu concentration, separated by three Al layers, were detected. The concentration change near the GP zones appeared to be somewhat more diffuse, and it is uncertain whether this is due to irregular evaporation behavior of Cu near the GP zones. More recent work using a 3DAP [31] succeeded in analyzing both GP zones and θ″ with a near-atomic resolution. Similar concentration–depth profiles were obtained. However, in that work, the diffuse character of the atom-probe concentration–depth profiles was attributed to evaporation artifacts, and it was suggested that the actual concentration of GP zones is close to 100 atomic percent (at. %) Cu.

The crystal structure of θ′ phase is well established [17] as a body-centred tetrago-

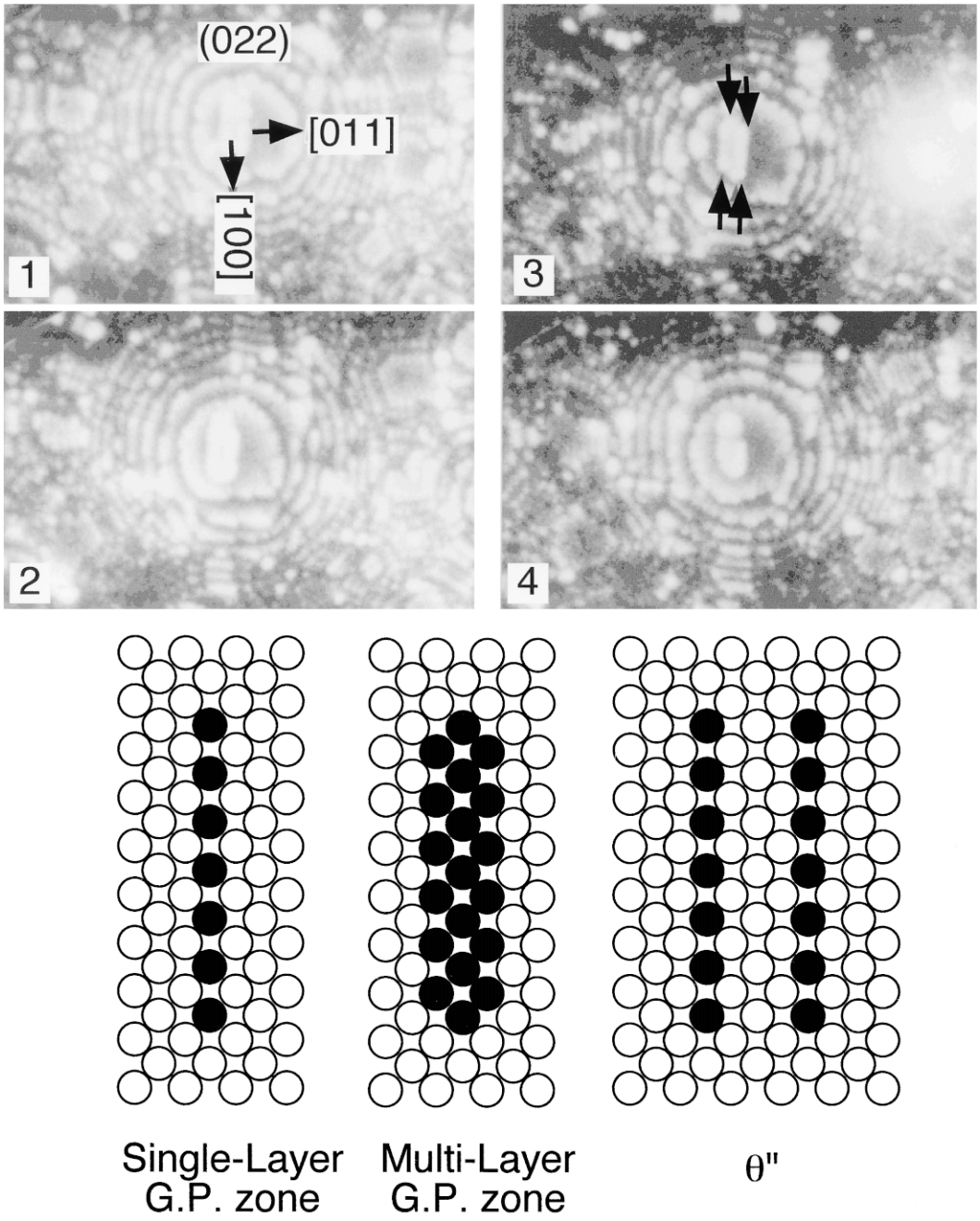

FIG. 3. (a) Field ion micrograph (Ne) sequence produced by field evaporation of four (1–4) successive $(022)_\alpha$ planes of an Al–1.7Cu alloy aged at 100°C for 300 min. (b)–(d) These represent schematic diagrams of the structure of single-layer GP zones, multilayer GP zones, and θ″ precipitation, respectively. After Hono et al. [11].

nal (I4/mcm, a = 0.404nm and c = 0.580nm), and occurs as octagonal-shaped platelets oriented such that $\{001\}_\alpha$ // $\{001\}_\theta'$ and $\{010\}_\alpha$ // $<010>_\theta'$ The morphology of these precipitates is accounted for using intersection point group symmetry analysis [32]. Because the above orientation relationship requires that all of the symmetry

elements of the θ′ phase are common to those of the m3m α-matrix, the intersection point group is the same as that of θ′ phase: 4/mmm. Because the point group of the matrix phase contains 48 symmetry elements and the intersection point group contains 16, the index of the intersection point group in the α-matrix is 48/16 = 3. Symmetry thus requires three crystallographically equivalent variants. The special crystal forms compatible with this point group [33] include pinacoids normal to the fourfold axis, and tetragonal prisms parallel to twofold axes possessing the required mirror symmetry, which is consistent with observation.

The tetragonal θ phase (I4/mcm, a = 0.6066nm, c = 0.4874nm) [34] occurs in a variety of orientations and morphologies. These have been systematically examined by Vaughan and Silcock, who showed that there are 159 known orientations for a θ particle relative to the α-Al matrix [35].

EFFECTS OF Sn, Cd, AND In ON PRECIPITATION IN Al–Cu ALLOYS

Trace additions of Cd, In, and Sn increase both the rate and extent of hardening in Al–Cu alloys aged at temperatures between 100 to 200°C [36–38] (Fig. 2). Comparisons between binary and ternary alloys have shown that, whereas these elements suppress the formation of the GP zones and the θ″ phase, they stimulate a finer and more uniform dispersion of the semicoherent θ′. Two types of proposals have been offered to describe the mechanisms for this refined precipitate dispersion. One hypothesis is that the trace elements are absorbed at the θ′/matrix interfaces, resulting in a reduction of the interfacial energy required for precipitate nucleation. This explanation was first proposed by Silcock et al. [37] to account for weak X-ray reflections (designated "p-diffractions") observed during the early stages of aging. This proposal received indirect experimental support from calorimetric measurements by Boyd and Nicholson [39] and TEM observations by Sankaren and Laird [40], who claimed to detect what they referred to as Sn (Cd or In) segregates and precipitates in association with the θ′ particle/matrix interface. An alternative explanation is that the trace elements facilitate heterogeneous nucleation of θ′ either directly at Sn (Cd or In)-rich particles [41–43], or indirectly at the dislocation loops present in the AQ microstructure [44].

Random area 1DAP analyses obtained from samples of an Al–1.7Cu–0.01Sn alloy indicate that the Sn atoms are not homogeneously distributed in the α-matrix immediately after quenching from the solution treatment temperature [45]. Rather, they occur in discrete clusters, and there was no evidence of enrichment of Cu at their locations. As is usual in the examination of AQ Al–Cu-based alloys, occasional clusters of Cu atoms were also observed, but these were not spatially correlated with the Sn clusters. A statistical test of the atom-probe data, known as contingency table analysis, also indicated that Cu and Sn did not have a preferential interaction in the clustering stage.

Figure 4(a) is an He FIM image of the Al–1.7Cu–0.01Sn alloy aged 3 min at 190°C and shows brightly imaging precipitates, indicated by arrows. The selected area 1DAP analysis presented in Fig. 4(b) was obtained by probing at or near these brightly imaging regions, which were found to be Cu-rich θ′ nuclei, heterogeneously nucleated on Sn particles. Figure 4(b) is an example of an analysis through the θ′/Sn interface. The Cu ladder is uniform through both the Sn particle and the adjacent matrix, confirming that there is no Cu enrichment in the particles. However, there is a sharp interface between the Sn-rich and Cu-rich precipitates. Note that in Fig. 4(b), the composition of the Cu-rich precipitate is ∼33 at. % Cu, which corresponds to the nominal composition of θ′ (Al_2Cu). This observation and the fact that Al and Sn have extremely limited solid solubility in each other suggest that the particles are pure Sn. Microbeam electron diffraction confirmed the presence of the β-Sn phase ($I4_1/amd$, a = 0.583nm, c = 0.318nm) oriented such that

$(100\}_{Sn}$ // $\{111\}_{\alpha}$ and $[010>_{Sn}$ // $<112>_{\alpha}$ [45]. [Mixed notation indices are used to represent planes (hkl} and directions [uvw> of tetragonal structures.] Figure 5 shows the microstructure after 1 h at 190°C, where it is seen that θ′ precipitates were often found associated with these particles, suggesting that they had provided sites at which heterogeneous nucleation of θ′ could occur. The Sn particles appeared to be incoherent with the Al matrix, because they were visible only through diffraction and structure factor contrast, and no strain was observed under two-beam conditions. The Sn particles are in contact with the narrow, noncoherent planes of θ′. Further 1DAP analyses revealed that Sn was not segregated to the θ′/matrix interfaces either across the coherent broad face of the θ′ plate or across the rim or edge. These results support the proposal by Kanno et al. [41–43] that Sn (Cd or In) facilitates precipitation of θ′ at elevated temperatures by providing heterogeneous nucleation sites. The rapid clustering and precipitation of Sn in this alloy has been explained in terms of evidence for a preferred Sn–vacancy interactions during, or immediately following, quenching, and the fact that the diffusion rate of Sn in Al may exceed that of Cu by at least two orders of magnitude [45].

Figure 6(a) shows an FIM micrograph of a general high-angle grain boundary in the Al–1.7Cu–0.01Sn alloy following aging 3 min at 200°C. Figure 6(b) shows an integrated concentration–depth profile across the grain boundary. The intragranular concentration of Cu determined from this data is significantly larger than the equilibrium solid solubility (∼0.1 at. %), and this is consistent with the observation that θ′ is in the early stages of precipitation. However, a Cu–solute-depleted region is evident in the region of the grain boundary, and there is no evidence of Sn segregation in the boundary. The solute depleted region was estimated to be ∼10nm thick. Narrow precipitate free zones (PFZ) approximately 0.1μm either side of the boundaries, to-

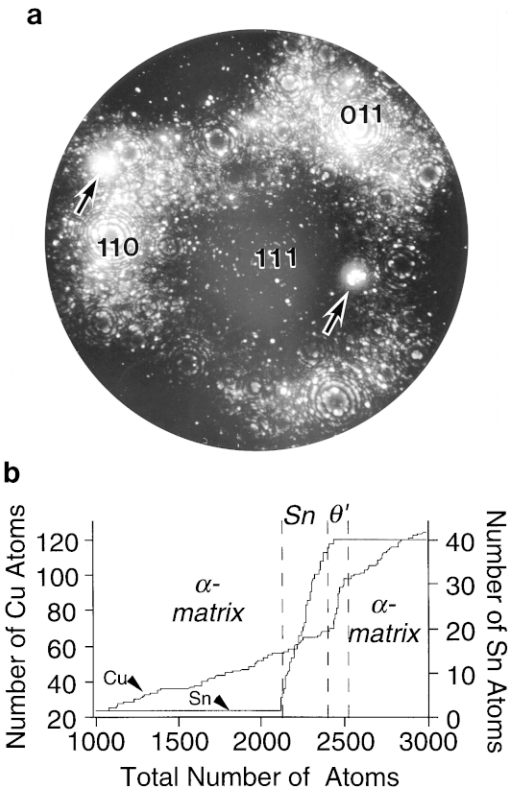

FIG. 4. (a) Field ion micrograph (He) from the Al–1.7Cu–0.01Sn alloy aged at 190°C, 3 min. The 1DAP results in (b) indicate that the brightly imaging regions are Cu-rich θ′ nuclei, heterogeneously nucleated on Sn particles. After Ringer et al. [45].

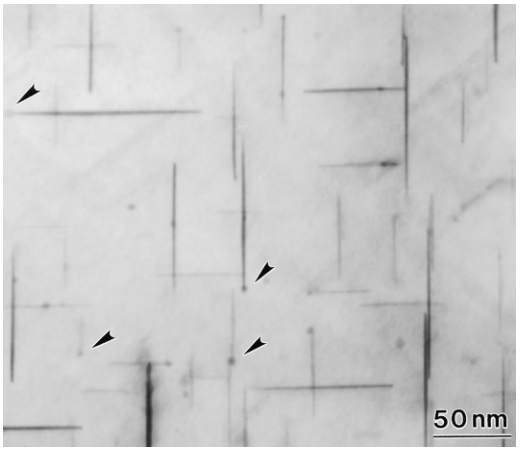

FIG. 5. Transmission electron micrograph of the Al–1.7Cu–0.01Sn alloy following aging for 1 h at 190°C. A fine and uniform dispersion of θ′ precipitates is seen, which are nucleated on spherical Sn particles (arrowed). After Ringer et al. [45].

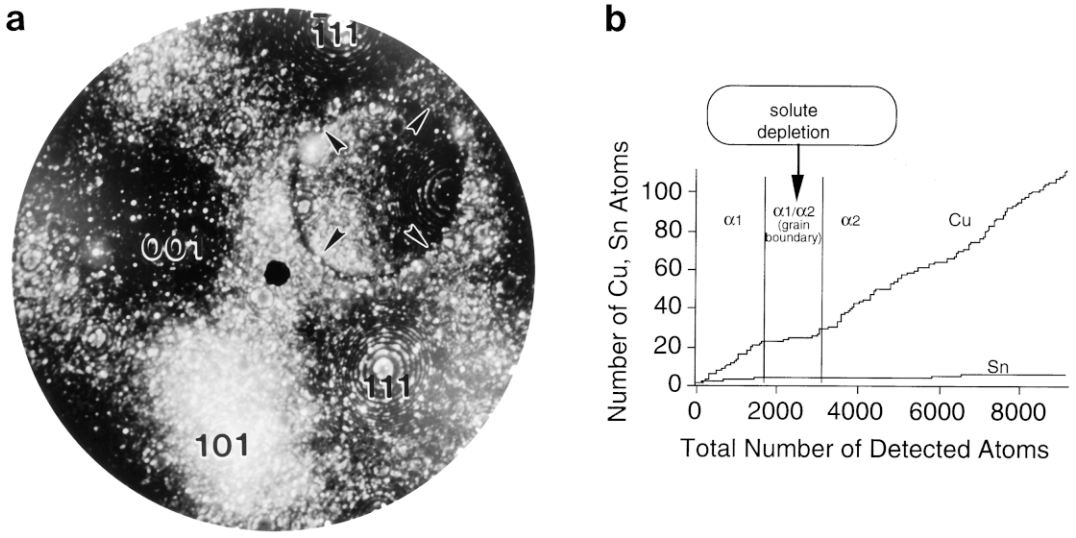

FIG. 6. (a) Field ion micrograph (He) of the Al–1.7Cu–0.01Sn alloy following aging for 3 min at 200°C. A grain boundary is arrowed. (b) Integrated concentration–depth profile resulting from probing across the boundary, showing solute depletion. After Ringer et al. [45].

gether with numerous large precipitates of the equilibrium θ phase (Al_2Cu) that had precipitated heterogeneously at grain boundaries were observed in BF TEM images from these alloys [45]. These observations suggest that the PFZs in these alloys result from both solute and vacancy depletion near the grain boundaries, as suggested by Geisler [46] and Varley et al. [47], unlike the Al–Zn–Mg alloys where the precipitate free zones are exclusively due to vacancy depletion [48, 49].

Al–Cu–Mg BASED ALLOYS

The range of microstructures, phases formed, and the response to microalloying in Al–Cu–Mg alloys is highly dependent on alloy composition (Fig. 7) [50]. The following discussion summarizes the results of recent studies on the microstructural mechanisms and evolution during aging in these alloys.

ALLOYS IN THE α + θ PHASE FIELD

Figure 8 is an hardness–time plot for the Al–1.7Cu–0.3Mg ternary alloy at 200°C, and includes curves for and Ag and Li containing alloys [51]. The data show that microalloying in both Al–Cu–Mg–Ag and Al–Cu–Li–Mg–Ag-based alloys is highly effective in enhancing the age hardening response. Indeed, high-strength Li-containing alloys possessing ultimate tensile strength exceeding 600MPa have recently been developed [52, 53].

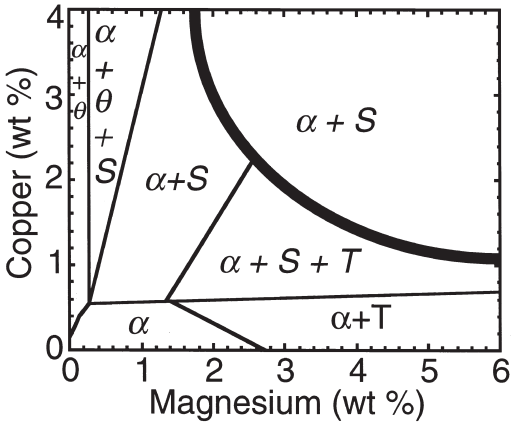

FIG. 7. Al–Cu–Mg phase diagram showing phase boundaries at 190°C. The thick solid line defines the α/α + S phase boundary at 500°C. After Brook [50].

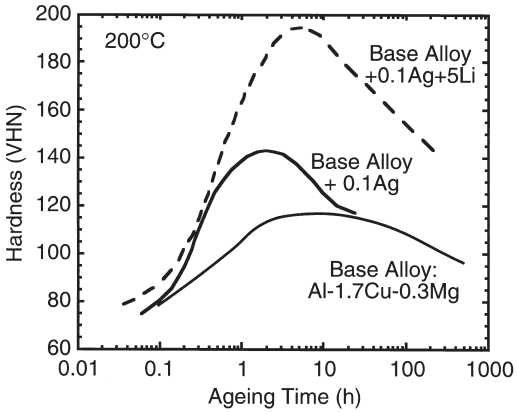

FIG. 8. Hardness–time plot for Al–1.7Cu–0.3Mg at 200°C, showing the effects of additions of Ag and Li. After Polmear and Chester [51].

Microstructural analysis using APFIM in conjunction with TEM is particularly useful in examining the very early stages of the precipitation process and for understanding the effects of microalloying. Figure 9(a) is a 1DAP-integrated concentration–depth profile of the ternary base alloy after aging 30 s at 180°C [54]. The data indicate a preferred interaction between Cu and Mg, in contrast to the AQ alloy samples, which indicated that the Cu and Mg were distributed independently. These results were supported by contingency table analysis, which indicated that there was no preferred interaction between Mg and Cu at the 99.6% confidence level. As suggested by the data in Fig. 9(a), the tendency of coclustering of Mg and Cu atoms was observed after aging for 30 s at 180°C. Independent Cu-rich clusters were also detected at this early stage of aging. The microstructure evolved after 2.5 h at 180°C consists of a fine and uniform dispersion of θ′ precipitation on the $\{001\}_\alpha$ planes together with GPB zones, which occur as rod-like features elongated along the cube directions of the matrix [Fig. 10(a)]. The term *GPB zones* was introduced by Silcock [55] in recognition of the XRD work on these rod-shaped zones by Bagaryatsky [56], who considered the zones to be associated with short-range ordering along the $\{100\}_\alpha$ planes. Silcock proposed that the zones formed along the $<100>_\alpha$ directions as small cylinders estimated to be 1 to 2nm in diameter, and with lengths ranging from 4 to more than 8nm, depending on quenching rate [55]. At 180°C, the microstructural evolution of the Al–1.7Cu–0.3Mg alloy is similar to that of binary Al–Cu. In addition, the Mg–Cu interaction results in the formation of GPB zones and prolonged aging at this temperature induces precipitation of the equilibrium S phase (Cmcm; a = 0.400nm, b = 0.923nm, c = 0.714nm) [57].

Effects of Ag Additions

The addition of Ag to Al–Cu–Mg alloys with high Cu:Mg ratios stimulates the formation of an hexagonal-shaped precipitate phase, designated Ω, which occurs on matrix {111} planes [58, 59]. Because the precipitation of Ω significantly improves the high-temperature strength of the Al–Cu–Mg base alloys, there have been numerous studies devoted to the determination of the crystallographic structure and composition of this phase [60–69]. The model proposed by Knowles and Stobbs [60] is widely accepted, and involves a face-centred orthorhombic structure (Fmmm, a = 0.496nm, b = 0.859nm, c = 8.48nm), having 12 crystallographically equivalent orientations described by the relation: $\{111\}_\alpha$ // $\{001\}_\Omega$, $[10\bar{1};]_\alpha$ // $[010]_\Omega$, $[1\bar{2}1]_\alpha$ // $[100]_\Omega$. Chang and Howe [64] have redesignated this phase as θ on the basis that it has the same composition as the equilibrium θ phase (Al_2Cu) found in Al–Cu alloys [34, 35], and they suggested that the precipitates have a tetragonal structure, based on convergent-beam electron diffraction (CBED) [62]. In either case, the differences in lattice parameter between the θ (tetragonal) and Ω (orthorhombic) structural models are extremely small, and prolonged aging at temperatures ⩾250°C results in the eventual replacement of the $\{111\}_\alpha$ Ω precipitates with the equilibrium θ phase (Al_2Cu) in a variety of orientations and morphologies [69].

The use of APFIM in studying the microstructural evolution of quaternary Al–1.7Cu–

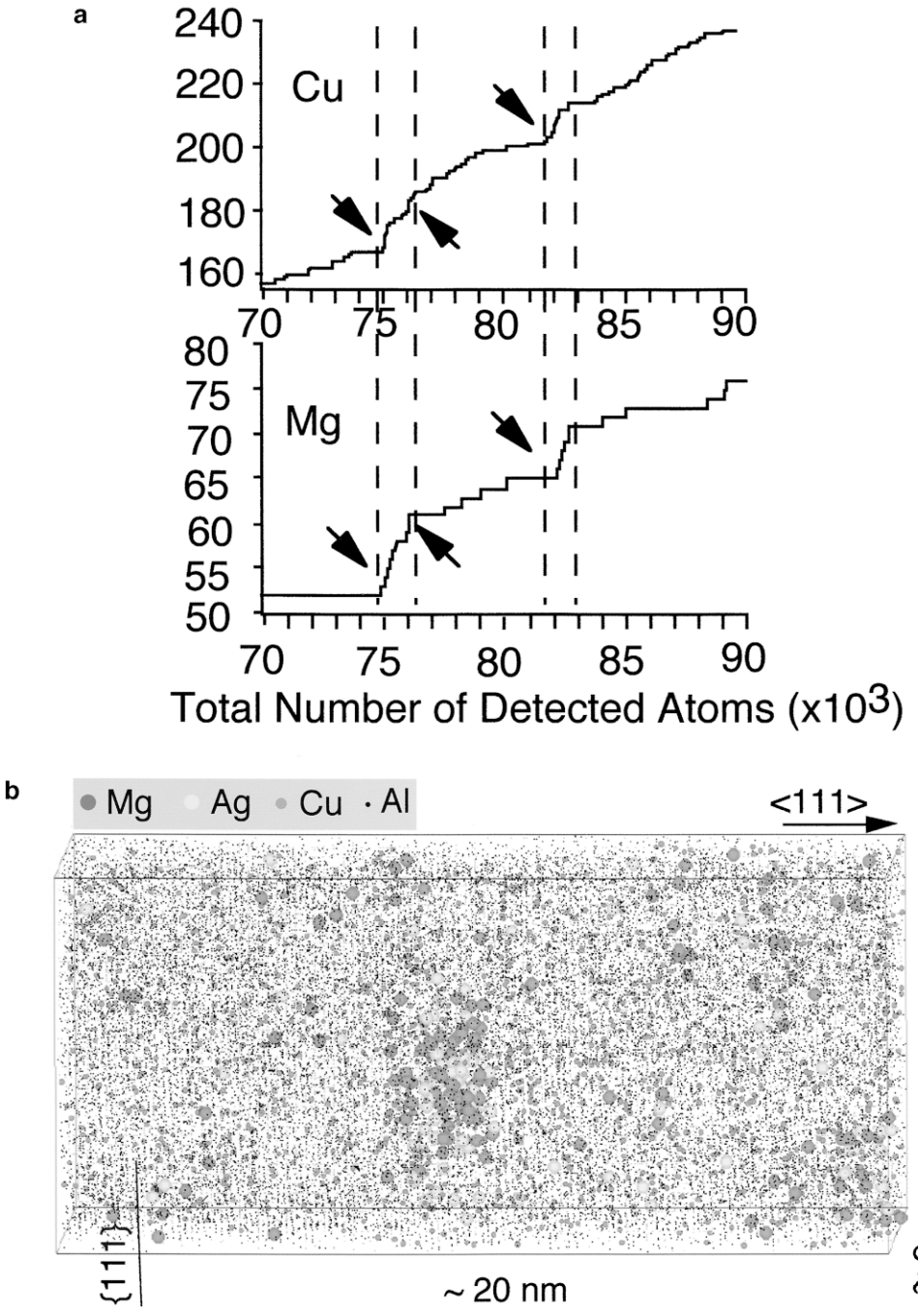

FIG. 9. (a) Integrated concentration–depth profiles (1DAP) from the ternary Al–1.7Cu–0.3Mg alloy after aging 30 s at 180°C. After Ringer et al. [54]. (b) Atomic reconstruction (3DAP) from the quaternary Al–1.7Cu–0.3Mg–0.2Ag alloy after aging 30 s at 180°C. After Reich et al. [72].

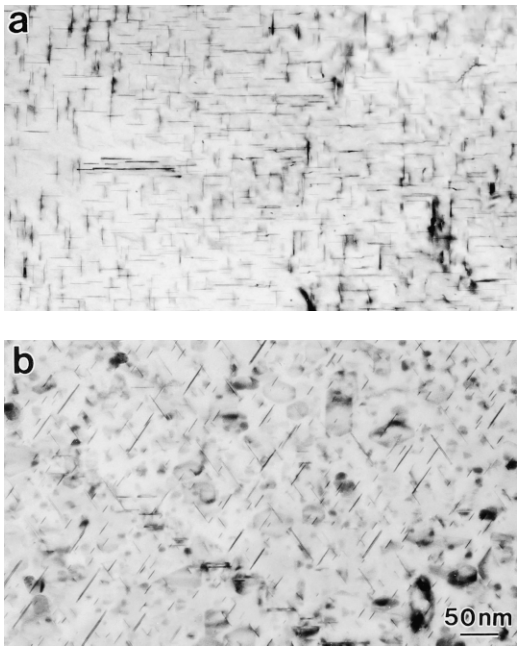

FIG. 10. Bright-field transmission electron micrographs showing the microstructure in (a) the ternary Al–1.7Cu–0.3Mg and (b) a quaternary Al–1.7Cu–0.3Mg–0.1Ag alloy after aging at 180°C for 2.5 h. The electron beam is parallel to <001>α and <011>α, respectively. After Ringer et al. [54].

0.3Mg alloys containing 0.1–0.2 Ag additions indicates that Ag modifies the precipitation process from the very earliest stages of the decomposition through a preferred Mg–Ag interaction [54, 70]. Recently, Murayama and Hono [71] and Reich et al. [72] reported further observations on how the Ω phase evolves from the solute clusters, using 3DAP. Figure 9(b) is an example of 3DAP elemental map of Mg, Ag, and Cu atoms in the Al–1.7Cu–0.3Mg–0.2Ag quaternary alloy aged for 15 s at 180°C [72]. The Ag and Mg atoms form a co-cluster involving ∼40–80 atoms. The shape of the co-cluster remains diffuse until subsequent aging causes the aggregation of Cu atoms to the cluster. At this stage, the clusters start to exhibit a distinct disc- or plate-like shape, with the habit plane parallel to the $\{111\}_\alpha$ planes. The microstructure evolved after 2.5 h at 180°C consists of a fine and uniform dispersion of Ω precipitation on the $\{111\}_\alpha$ planes together with θ′ platelets on the $\{001\}_\alpha$ planes [Fig. 10(b)]. Figure 11 is a 3DAP reconstruction of a coarsened Ω platelet observed in the specimen aged for 10 h at 180°C [72]. The Ω precipitate is observed edge-on, and a ledge is observed clearly. The thickness of the platelet may be estimated from the resolved atomic layers of the matrix phase, and was approximated as 10–13 $\{111\}_\alpha$ layers, which corresponds to three unit cells of Ω. Whereas Ag and Mg atoms are absent from the interior of the Ω phase precipitate, they are strongly segregated to

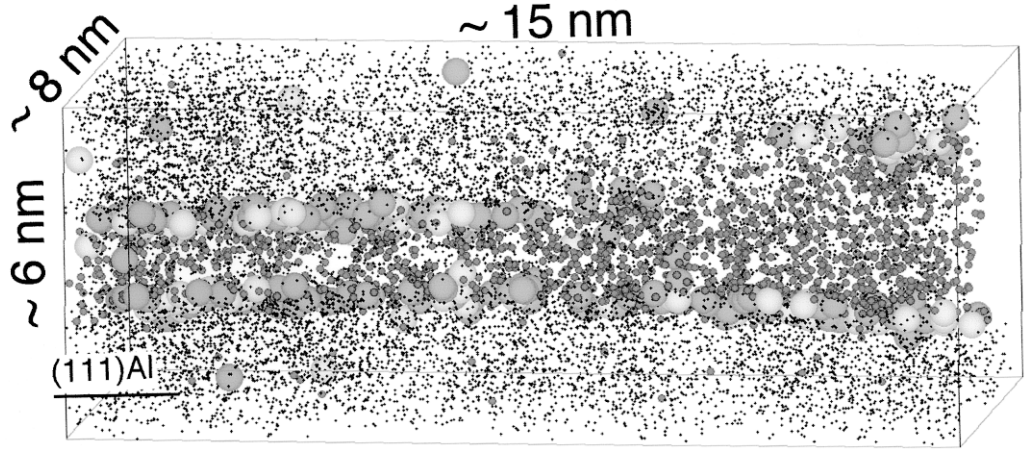

FIG. 11. Three-dimensional reconstruction (3DAP) of the atomic-scale chemistry of an Ω precipitate viewed edge-on in quaternary Al–1.7Cu–0.3Mg–0.2Ag alloy after aging at 180°C for 10 h. The finer dots represent Al atoms, the large spheres represent Ag, the small dark spheres Cu, and the large dark spheres represents Mg. After Reich et al. [72].

the broad Ω/α interface. The segregated region is restricted to one or two layers, and no Mg atoms are incorporated within the precipitate. The Cu concentration of the interior of the precipitate is approximately 33 at. % Cu, which matches with the composition Al_2Cu. The data clearly support the conclusions of earlier work [61, 65, 68] that Ag and Mg are segregated to the broad (habit) facet of the Ω phase. It is interesting to observe the flux of Cu atoms from the ledge. It is thought that this derives from the dissolution of the platelet, which is participating in a coarsening reaction.

The observations of Mg–Ag co-clusters suggest that the role of Ag is to effectively trap Mg atoms, resulting in the formation of numerous Mg–Ag co-clusters, which act as potent nucleation sites for the Ω phase [54, 70]. A similar proposal was made by Chang [63] to account for what he considered was the catalytic action of Mg and Ag, and the recent 3DAP work by Reich et al. [72] further confirms that Ω phase nucleates from Mg–Ag coclusters. It is thought that the Mg–Ag coclusters promote the formation of $\{111\}_\alpha$ Ω precipitation by relieving the slight lattice distortion that differentiates this structure from the tetragonal θ unit cell. This reduces the precipitate–matrix lattice misfit and facilitates coherent precipitation on $\{111\}_\alpha$. The observation that the Ω/α orientation relationship is rational, whereas the Vaughan II θ/α relationship is found experimentally to be irrational, supports this view [69]. The Vaughan II orientation was initially proposed on the basis of lattice matching as a rational relationship, where $(\bar{1}10)_\theta$ // $(111)_\alpha$, $[110]_\theta$ // $[10\bar{1}]_\alpha$ [35]; however, there are no published examples of θ phase in this orientation in Al–Cu alloys. On the basis of experimental observations [69], it has been proposed that θ phase precipitates in orientations that are, in fact, slightly rotated from this rational relationship. Several proposals based on the relative atomic sizes of Mg, Ag, Al, and Cu have been put forward to explain how this mechanism might operate at the Ω/α interface [54, 65, 71]. All involve the larger atomic size of Mg reducing the >9% lattice contraction normal to the habit plane. Suh and Park [73] recently showed that Mg–Ag coclusters form preferentially on $\{111\}_\alpha$ planes due to strain energy considerations. This is consistent with the $\{111\}_\alpha$ GP zones observed by Ciu et al. [74, 75] and Reich et al. [72]. Recently, Karlik and Jouffrey [29] observed GP zones in binary Al–Cu alloys on $\{111\}_\alpha$ planes. Although the formation of these zones is clearly a relatively rare occurrence in Al–Cu, it is possible that such features may be stabilized by the Mg–Ag co-clusters that precede them.

This interpretation also explains the observation that Ω forms only as a minor phase in ternary Al–Cu–Mg alloys [66, 67], because the tendency for the formation of suitably large Mg clusters is diluted by weaker interactions and the tendency to form Mg–Cu co-clusters [54]. It is likely that the chemical nature of the Mg–Cu coclusters is different from that of the Mg–Ag co-clusters in the quaternary alloy. Apart from valence effects, the atomic size of Cu is significantly smaller than Al, Ag, or Mg, and it would be unlikely to promote $\{111\}_\alpha$ Ω precipitation in the manner proposed above, because the larger size of Mg and the smaller size of Cu would tend to have a minimal net size effect. Thus, in the ternary Al–Cu–Mg alloy, the Cu clusters are likely to grow as GP zones; some of the Mg–Cu clusters are believed to grow as GPB zones, while some of the Mg clusters do seem to nucleate Ω.

Effects of Ag + Li Additions

The combined addition of Ag and Li to Al–1.7Cu–0.3Mg alloys results in a high level of hardening, with an optimum content at ~5 at. % Li [51]. This observation led to the development of new, ultrahigh strength alloys known as the Weldalite™ series [53]. Various studies have shown that Ag + Li additions to Al–Cu–Mg alloys promote a fine and uniform precipitation of the T_1 phase, which occurs on matrix $\{111\}_\alpha$ planes [51, 53, 77–84]. Some controversy exists over the structure of this phase, al-

though most proposals involve a hexagonal unit cell [76–78] with composition Al_2CuLi. Lee et al. [79, 80] and Huang and Zheng [81] have shown that the Ω phase predominates the microstructure of aged alloys containing Li levels <2.5 at. %, and that the T_1 phase predominates in alloys containing between ~2.5 and ~5 at. % Li. Further Li additions stimulate copious precipitation of the δ′ (Al_3Li) phase. A 1DAP analysis of the T_1 phase is shown in Fig. 12. This shows that Mg and Ag are associated with the T_1 precipitate, which is consistent with the EDXS [79] and other 1DAP analyses [82]. The composition of the T_1 phase appears reasonably close to Al_2CuLi. Moreover, it is apparent that Mg and Ag are segregated to the T_1/α interphase interface. This has been further confirmed by recent 3DAP analyses [83]. There are at least two obvious similarities between the effects of Ag additions on the precipitation of T_1 and Ω in Li containing and Li free Al–Cu–Mg alloys, respectively: (i) uniform precipitation of these $\{111\}_\alpha$ precipitates occurs only when Mg is present, while the addition of Ag further refines their dispersion; and (ii) these elements are segregated to the particle/matrix interphase interface. This suggests that the way in which Mg and Ag stimulate the uniform dispersion of the T_1 may be the same as that previously discussed for the Ω phase.

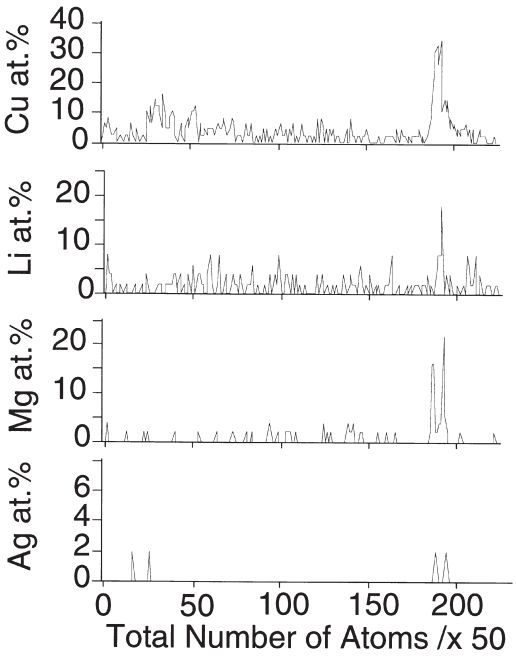

FIG. 12. Concentration–depth profiles (1DAP) from an Al–5Li–2.25Cu–0.4Mg–0.1Ag–0.04Zr alloy, known commercially as Weldalite™ 049, after aging for 2 h at 200°C. The data indicates the association of Mg and Ag with the T_1 phase, and shows that these elements are segregated to the particle–matrix interface.

ALLOYS IN THE α + S PHASE FIELD

These materials remain as one of the two major classes of aluminium alloys (2000 series) used for aircraft construction world wide [1, 84]. Figure 13 is a hardness–time plot for the Al–1.1Cu–1.7Mg alloy at 150°C showing the effect of a 0.1 Ag addition. Isothermal aging of these alloys and their commercial counterparts such as AA2618 and AA2024 reveals several interesting features (Fig. 13): (i) hardening occurs in two distinct stages separated by a plateau during which time the hardness remains constant for many hours [85]; (ii) the first stage of hardening occurs very rapidly, and is largely complete within 60s; and (iii) some 60% of the total hardening during aging (peak hardness minus the AQ hardness value) occurs during this rapid first stage. The last two features are not widely realized, particularly in commercially heat-

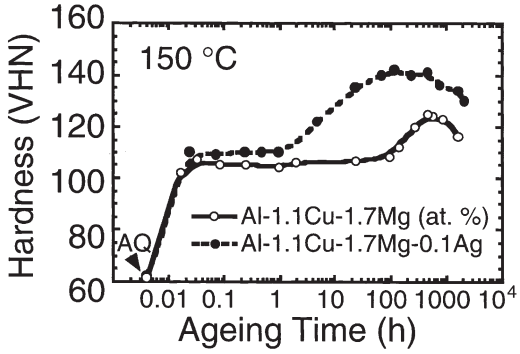

FIG. 13. Hardness–time plots for the Al–1.1Cu–1.7Mg alloy aged at 150°C, showing the effects of Ag additions. After Ringer et al. [87].

treated alloys, because accurate values of AQ hardness are often not determined. The first stage of hardening in Al–Cu–Mg alloys has generally been attributed to the formation of GPB zones, while the second stage of hardening has generally been attributed to the formation of the S′ or S phase [55, 85].

Recent work proposed a different interpretation of the origins of hardening in this alloy [86–88]. The microstructural evolution during aging after solution treatment is considered to involve the following processes:

1. Immediately following quenching, a rapid coalescence of quenched-in vacancies occurs, resulting in vacancy condensation and the formation of a large number of dislocation loops. The loops lie on the $\{110\}_\alpha$ planes and possess $a/2 <110>_\alpha$ Burgers vectors [49, 89].
2. Within seconds of aging at elevated temperatures, a rapid hardening reaction occurs. This is thought to be related to a subtle redistribution of the solute through a preferred interaction between Mg, Cu, and dislocations. The term cluster hardening was recently introduced to describe this phenomenon [86, 87].
3. The diffusion of Mg and Cu atoms to the dislocation loops and helices which leads to heterogeneous precipitation of the S phase at these defects [87, 88, 90, 91]. Once formed, these precipitates persist throughout the subsequent aging sequence.
4. Towards the end of the hardness plateau, a fine and uniform precipitation of GPB zones occurs [87, 88]. The onset of precipitation of the GPB zones (Figs. 14 and 15) causes a second increase in hardness, which reaches a maximum when the zones occur in a critical dispersion [92].
5. Overaging occurs as the GPB zones are gradually replaced by matrix precipitation of the S phase, which grows progressively coarser [87].

Observations using CTEM and HRTEM show no evidence of matrix precipitation in an Al–1.1Cu–1.7Mg alloy in either the AQ condition or after aging at 150°C for 5 min, that is, just before and after the rapid hardening reaction. Similarly, APFIM of the alloy in the AQ condition detected independent Mg clusters and Cu clusters with no evidence of precipitation. Figure 16 provides 3DAP data [92] from the Al–1.1Cu–1.7Mg alloy after aging for 5 min at 150°C, and maps the spatial distribution of Cu and Mg atoms and confirms that the formation of zones or precipitates has not occurred within this short aging time [86–88, 90–91]. However, in contrast to earlier reports, based on 1DAP data [86, 87], the 3DAP results reveal little or no evidence of a uniform distribution of Cu–Mg coclusters throughout the matrix. This illustrates how the larger volume of sample acquired in 3DAP provides a unique and critical insight into alloy microstructure. Random-area 1DAP analyses [86, 87] reported slight differences in the Cu–Mg distribution between samples in the AQ condition and samples aged 5 min at 150°C. Whereas this was interpreted as evidence of a uniform distribution of Cu–Mg coclusters, the 3DAP results suggest that a preferred Cu–Mg interaction is clearly not an effect that is

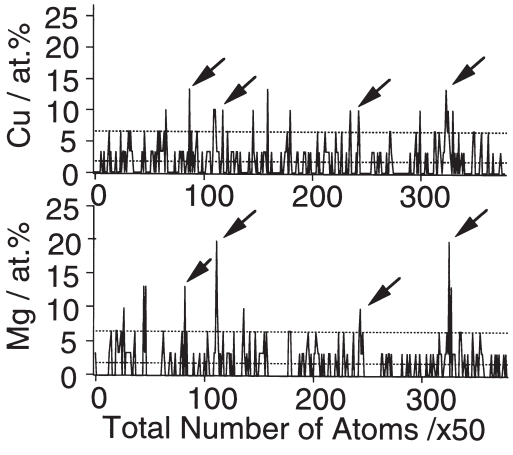

FIG. 14. Concentration–depth profiles (1DAP) from the ternary Al–1.1Cu–1.7Mg alloy aged to the end of the hardness plateau (150°C, 100 h), showing coenrichment of Cu and Mg at GPB zones. After Ringer et al. [87].

observed *uniformly* throughout the matrix, suggesting that there is another, previously unconsidered, aspect to these interactions. Recent work suggests that the disparity between the previous 1DAP results and recent 3DAP data (Fig. 14), arises because the Cu and Mg atoms cluster at the sites of the quenched-in defect structure and so occur in a distinctly *non-uniform* dispersion [88]. This eventually leads to the heterogeneous precipitation of the S phase at these dislocations [87, 88, 90, 91, 93–96]. The rapidity of this heterogeneous precipitation increases with increasing aging temperature and supersaturation [88, 90]. Significantly, the heterogeneous precipitation of the S phase proceeds after the rapid hardening [87, 88]. This suggests that the mobile dislocations that were available in the AQ specimens are pinned or locked by solute forming a

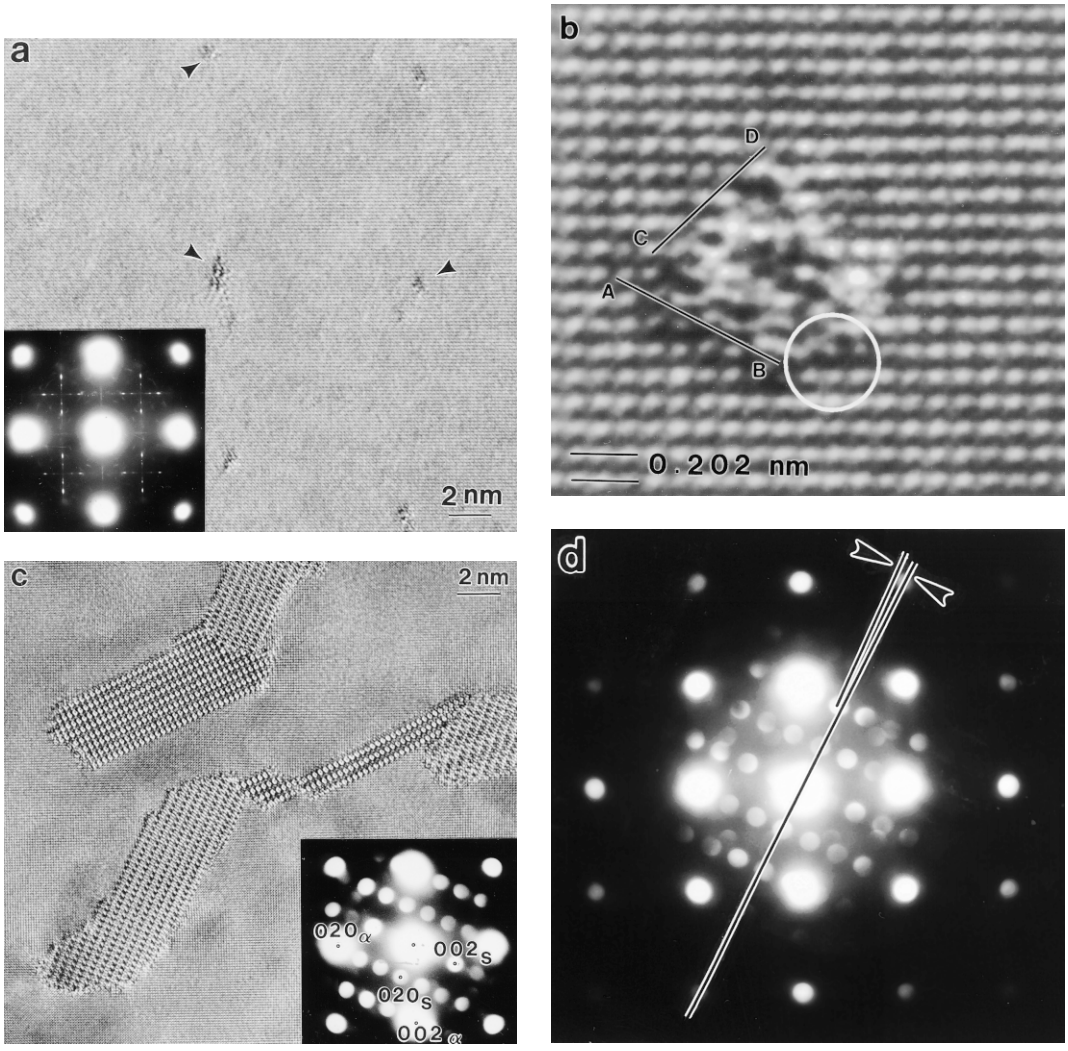

FIG. 15. High-resolution transmission electron micrographs from the peak hardness microstructure of the Al–1.1Cu–1.7Mg alloy (aged 500 h at 150°C). (a) GPB zones and a general SAED pattern (inset), (b) digitized and enlarged view of a typical zone showing the development of facets labeled AB and CD, approximately parallel to $\{210\}_\alpha$ and $\{110\}_\alpha$, respectively; some elastic distortion of the α-matrix is also circled, (c) S precipitates, as viewed in the $<001>_\alpha$ orientation together with a typical microbeam electron diffraction patterns (inset). (d) Microbeam electron diffraction pattern showing the α/S lattice rotation. After Ringer et al. [87, 94].

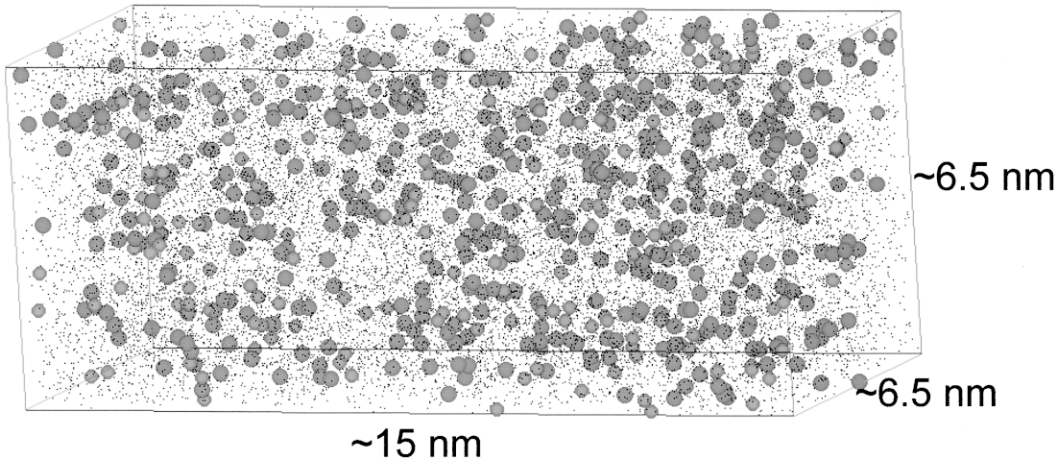

FIG. 16. Three-dimensional reconstruction (3DAP) of the solute distribution in the ternary Al–1.1Cu–1.7Mg alloy following aging for 5 min at 150°C. Dark spheres represent Cu, light spheres represent Mg, and the fine dots represent Al atoms. After Ringer et al. [92].

sessile dislocation network. Therefore, the rapid hardening effect appears to have origins that are distinctly different from those usually attributed to precipitation hardening effects.

Recent results indicate that this hardening is also stimulated by deformation such that a thermomechanical cycle involving short-term aging $\rightarrow$ deformation $\rightarrow$ short-term aging after initially quenching from the solution treatment temperature can cause hardening at both aging steps [89]. This thermomechanical sequence is thought to evolve as follows: the initial age-hardening derives from the Mg–Cu solute interaction with dislocations, which rapidly become locked by solute atoms and form a sessile dislocation network. The deformation subsequently generates new dislocations that are thought to interact with and become locked by Cu–Mg solute atoms during the second aging step, resulting in an extended sessile dislocation network and, therefore, a second hardening increment.

Near the end of the hardness plateau, uniform precipitation of GPB zones was observed [87, 88], and Fig. 15 provides typical concentration–depth profiles, which suggest that the zones contain approximately equal numbers of Cu and Mg atoms. It should be noted that the kinetics for the GPB zone formation are extremely slow compared to those for other GP zones observed in most other aluminium alloys. This suggests that most of the quenched-in vacancies were condensed before or during the rapid hardening process, and it is this process that leads to the formation of numerous dislocation loops in the AQ microstructure. It is thought that the rapid condensation of quenched-in vacancies also provides a mechanism for the transport of solute to these sites due to a preferred interaction involving Cu, Mg, and vacancies. The localized vacancy condensation at the start of the decomposition sequence retards the kinetics of the subsequent precipitation of GP zones.

Regarding the precipitation of the S phase, it is noteworthy that MBED analysis provided results that were consistent with the Perlitz-Westgren structural model [57], and the following orientation relationship has been observed [94]:

$$[100]_s // [100]_\alpha$$

$$[100]_s // [0\bar{2}1]_\alpha$$

$$[100]_s // [012]_\alpha$$

These results suggest a slightly different particle morphology to that deduced by Wilson and Partridge [95], who proposed

that the broad facet of the lath was the $(010)_S$ plane, based on matching of the periodicity of the two lattices. Inspection of Fig. 16(c–d) shows that the broad facet of the lath is, in fact, $(001)_S$, and similar conclusions were drawn from HRTEM studies [63]. Recently, it was also reported that the habit plane of the lath arrowed at the right of Fig. 16(c) can be rotated several degrees from $\{210\}_\alpha$ [94]. A slight rotation between the S-α lattices has been recorded in many MBED patterns, implying an irrational orientation relationship where $(001)_S$ is rotated between 2 and 3 degrees from $(0\bar{2}1)_\alpha$ around $[100]_\alpha$ [Fig. 16(d)]. This effect is not exclusive to precipitates with certain sizes or nucleation sites, and seems to be a feature of equilibrium precipitates in Al-based alloys, because it is consistent with the occurrence of multiple orientation relationships and morphologies for the θ phase in Al–Cu alloys and the η phase in Al–Zn–Mg alloys.

Finally, it may be noted that the evidence for the existence of intermediate phases that warrant the introduction of nomenclature such as S″ or S′ does not appear to be conclusive. Recent MBED [91, 94] and SAED [96] studies suggest that there is no justification for differentiating these precipitates from the equilibrium S. Here it may be noted that the reflections attributed to S″ by Ratchev et al. [90] are coincident with the oxide film reflections known to form in Al alloys [97].

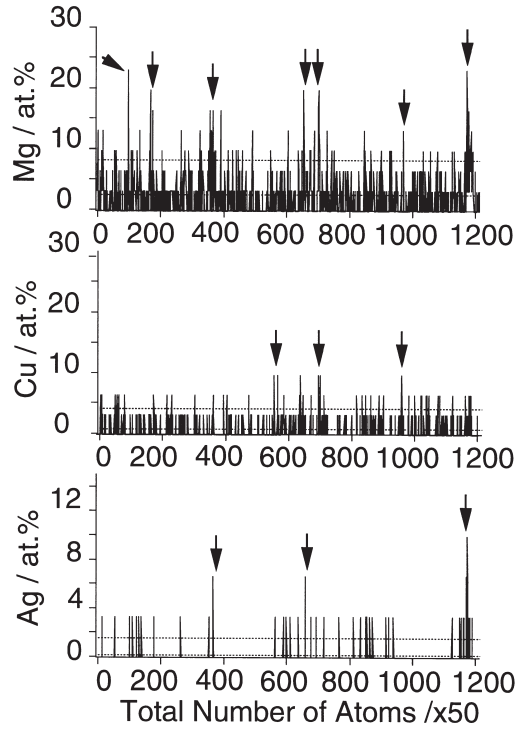

FIG. 17. Concentration–depth profiles (1DAP) from an Al–1.1Cu–1.7Mg–0.1Ag alloy after aging 5 min at 150°C. Individual and coclustering of Cu, Mg, and Ag solute atoms was detected (arrows). After Ringer et al. [87].

Effects of Ag Additions

Figure 13 indicates that the addition of Ag to the base alloy does not affect the characteristics of the hardness–time curve [85, 87]. The effect of Ag is to increase the rate of hardening, and it is noted that the hardness plateau is shorter, as is the time-to-peak hardness. Figure 17 is a selection of 1DAP data from an Al–1.1Cu–1.7Mg–0.1Ag alloy after 5 min at 150°C [87]. The concentration–depth profiles show that clusters of Mg atoms, Mg–Cu coclusters, and Mg–Ag coclusters are all detected. Among these, the Mg–Ag coclustering is particulary notable, given that such features have been associated with $\{111\}_\alpha$ precipitation in the foregoing discussion. A MBED study by Chopra et al. [98] has shown that a $\{111\}_\alpha$ phase, designated X′, forms in the Al–1.1Cu–1.7Mg–0.1Ag alloy, possessing an hexagonal structure (a = 0.496nm, c = 1.375nm), and oriented such that $(00.1)_{X'}$ // $\{111\}_\alpha$, $[10.0]_{X'}$ // $<110>_\alpha$. Figure 18(a) is a $<110>_\alpha$ BF TEM image recorded from the Al–1.1Cu–1.7Mg–0.1Ag alloy after aging at 200°C for 1 h. Edge-on variants of the X′ phase are clearly seen on both sets of the $\{111\}_\alpha$ planes, which are parallel to the electron beam in this orientation. Figure 18(b) is a concentration–depth profile from a selected area 1DAP analysis showing the composition of the X′ phase. The concentrations of Cu and Mg in X′ were fairly similar, and Al is the major constituent. The composition of X′ was determined to be

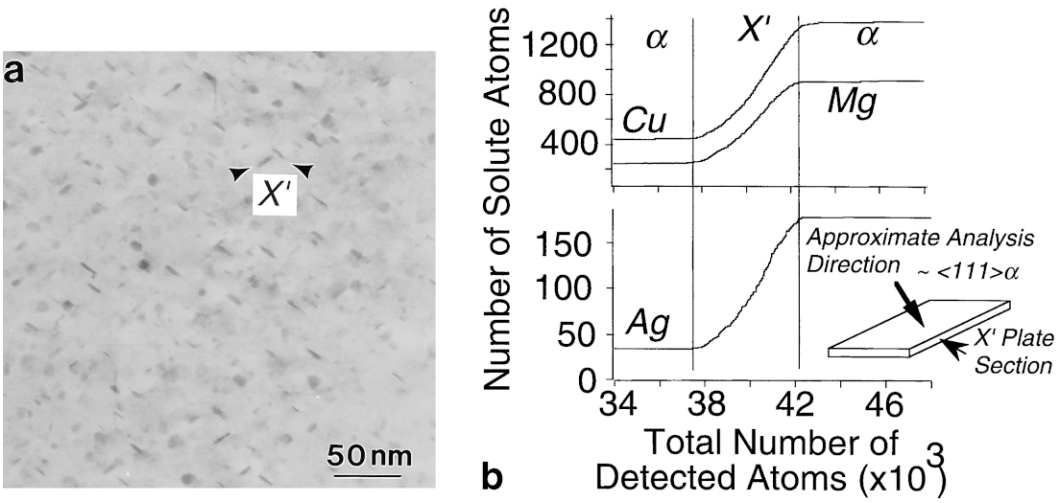

FIG. 18. Analysis of Al–1.1Cu–1.7Mg–0.1Ag alloy after aging for 1 h at 200°C. (a) $<001>_{\alpha}$ bright-field transmission electron micrograph; (b) integrated concentration–depth profile (1DAP) and schematic representation of the analysis mode. After Ringer et al. [87].

50–65 at. % Al 20–25 at. % Cu, 15–25 at. % Mg, with a maximum of 5 at. % Ag, implying a ratio of Al:Cu:Mg of approximately 2:1:1, which is similar to the S phase. The fact that the integrated concentration–depth profiles also revealed that Ag is contained *inside* the X′ precipitate is contrary to the situation with the Ω phase and the T_1 phase, where Mg and Ag are segregated to the precipitate/matrix habit interface. This difference in the location of Ag in these precipitates may be explained in terms of their respective compositions. Because of the strong interaction between Mg and Ag, it is expected that Ag accompanies Mg into the X′ phase during nucleation and growth, particularly as Ag atoms may substitute for Al atoms because of their similar atomic sizes. On the other hand, because Mg is not a constituent element of either Ω phase (Al_2Cu) or T_1 phase (Al_2CuLi), segregation of Ag and Mg to the precipitate–matrix interface occurs during growth.

ALLOYS IN THE α + S + T PHASE FIELD

The alloys within the α + S + T phase field have slow rates of softening at elevated temperatures. However, their commercialization has been limited due to the fact that their tensile strengths are no greater than alloys containing less Mg, when tested at temperatures ranging from 150–200°C. In this regard, Ag additions have been effective in enhancing the age-hardening response in this alloy system [85]. Figure 19 is an hardness–time plot for Al–0.64Cu–4.7Mg and Al–0.64Cu–4.7Mg–0.1Ag alloys. The hardening characteristics are very similar to those for the alloys in the α + S phase field, and although it may seem reasonable to assume that similar hardening mechanisms operate, very little characterization work has been completed on the base ternary alloys in this phase field. The T phase (Al_6CuMg_4, T_5^h, a = 1.425nm) is regarded as isomorphous with the T phase, which forms in Al–Zn–Mg alloys [99, 100].

Effects of Ag Additions

As with Al–Cu–Mg alloys in the α + S phase field, the addition of Ag has little effect on the character of the hardness–time plot [85, 101]. The rate of hardening is again increased; however, the level of the initial rapid hardening reaction is significantly raised. The Ag-containing alloys have been studied in more detail than the base alloys

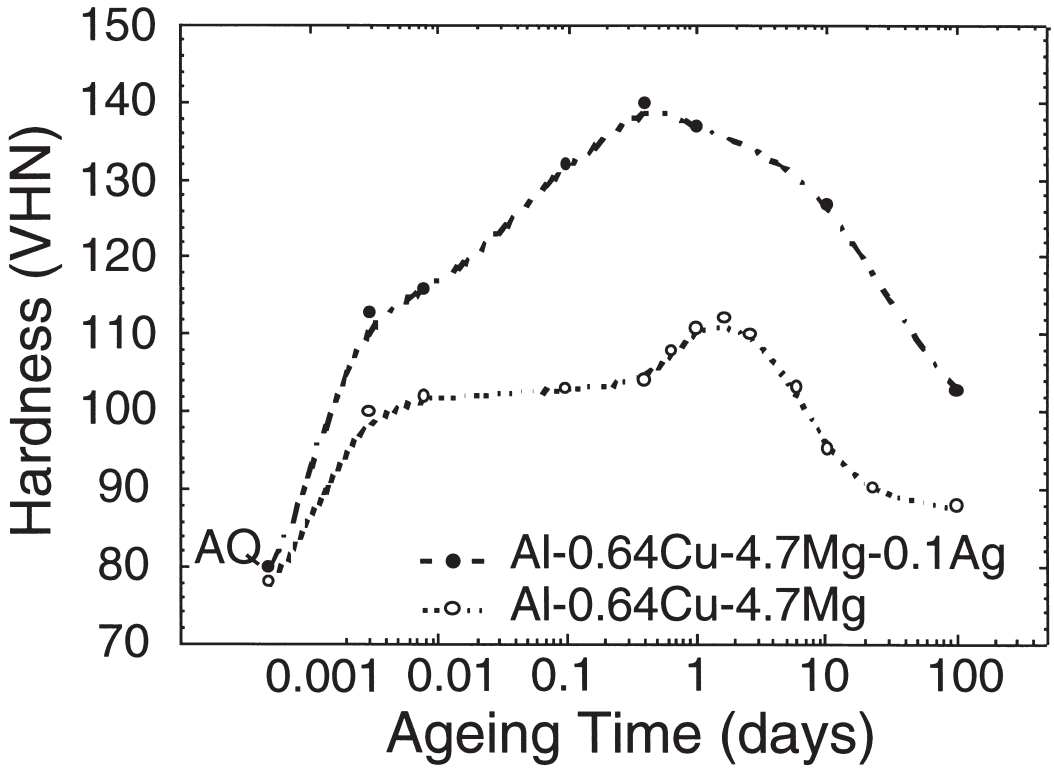

FIG. 19. Hardness–time plots for the Al–0.64Cu–4.7Mg alloy aged at 200°C, showing the effects of Ag additions. After Ringer et al. [101].

in this region of the Al–Cu–Mg phase diagram. Vietz and Polmear [85] concluded that Ag caused a refinement in the dispersion of the T phase, which appeared to be equiaxed in morphology. The precipitate was particularly resistant to coarsening, and this is apparent from the hardness–time data (Fig. 19) and the microstructures published by Vietz and Polmear [85]. A recent MBED study by Chopra et al. [102] indicates that the precipitates in the Ag-modified alloy are not, in fact, isomorphous with the T phase. They proposed that the microstructure of the Ag containing alloy is dominated by a phase, designated Z, which possesses a cubic structure (m3m, a = 1.999nm) and identified two orientation relationships with the α-matrix: $(100)_Z$ // $(100)_\alpha$, $[010]_Z$ // $[010]_\alpha$ and $(011)_Z$ // $(111)_\alpha$, $[0\bar{1}\bar{1}]_Z$ // $[0\bar{1}\bar{1}]_\alpha$. It is noteworthy that the effect of Ag again stimulates the formation of a refined precipitate dispersion.

Figure 20(a) is a $<100>_\alpha$ BF TEM image of the peak hardness (200°C, 9 h) microstructure of the Al–0.64Cu–4.7Mg–0.1Ag alloy, and Fig. 20(b) is typical data taken from selected area 1DAP analysis of the Z precipitates [101]. The analysis was performed with the probe hole near the $\{111\}_\alpha$ pole, and it is seen that a precipitate was cut by the cylinder of analysis. Figure 20(b) clearly shows that Ag was associated with the Z phase, and indicates that the concentration of Mg is generally higher than that of Cu, and that Al is the major constituent of the phase. The average composition of Z was determined to be 20 at. % Cu, 20–25 at. % Mg, and 50–65 at. % Al, implying a Cu:Mg ratio of approximately 4:5. The analysis of a number of precipitates clearly indicated that Ag was contained *inside* the Z precipitate in concentrations ranging from ~2–5 at. %.

It is proposed that the explanation for the incorporation of Ag within the lattice of the

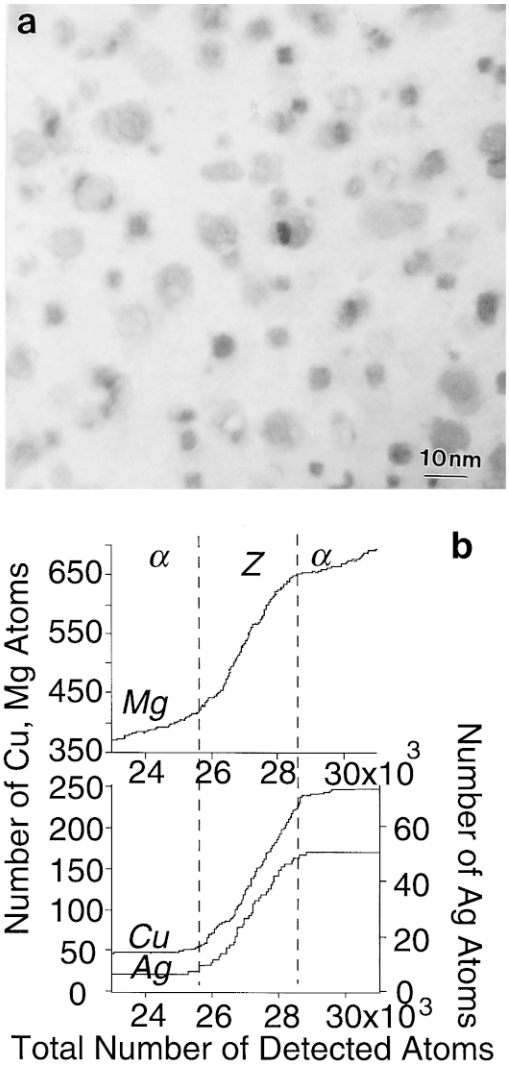

FIG. 20. Analysis of Al–0.64Cu–4.7Mg–0.1Ag alloy after aging for 9 h at 200°C. (a) $<001>_{\alpha}$ bright-field transmission electron micrograph; (b) integrated concentration–depth profile (1DAP) and schematic representation of the analysis mode. After Ringer et al. [101].

Z precipitate is similar to that proposed for the X′ phase [$Al_2CuMg(Ag)$] in the Al–1.1Cu1.7Mg–0.1Ag alloy. Because both the X′ and Z phases are rich in Mg, it is seems reasonable that Ag is also drawn into the precipitate lattice due to the Mg–Ag affinity. A similar process occurs when Ag is incorporated into the S phase (Al_2CuMg) in overaged Al–1.7Cu–0.3Mg–0.1Ag alloys [69].

Al–Mg–Si BASED ALLOYS

The 6000 series alloys are widely used as medium-strength structural alloys. Their weldability, corrosion resistance, and formability makes these alloys candidate materials for automobile body sheet applications. The extremely fine scale of the precipitation products in these alloys has long been realized [103, 104]. Based on DSC and CTEM results, Dutta and Allen [105] recently proposed the precipitation sequence in this alloy system as:

$$\text{SSSS} \rightarrow \text{solute clusters} \rightarrow \text{GP zones (spherical)} \rightarrow \beta''(\text{needle}) \rightarrow \beta'(\text{rod}) \rightarrow \beta$$

where β is the equilibrium phase Mg_2Si. Three decades ago, Pashley et al. [104] reported that the number density and the size of the precipitation products in the peak hardenss condition are highly sensitive to the preaging condition in two-step aging, and they proposed a kinetic model to explain their microstructural observations under various heat treatment conditions. Until recently, this two-step aging process was mostly of scientific interest. However, renewed interest in this process has been stimulated by the possibility of using these alloys for automobile body sheet, where age hardening is carried out during the paint–bake cycle (∼30 min at 175°C). In this application, the alloys for are used in the underaged condition. Alloys containing an excess amount of Si from the Al–Mg_2Si quasibinary composition have been found attain satisfactory levels of hardness during this restricted aging period [106]. However, this hardening response is largely suppressed when the alloys are naturally aged for prolonged periods of time after solution treatment. To understand and overcome these problems, much effort is currently devoted to study the precipitation processes of Al–Mg–Si-based alloys.

The early stages of the artificially aged 6061 alloy were investigated recently by Edwards et al. [107]. In that work, APFIM and TEM were used to show that the initial stages of decomposition involve the sepa-

rate clustering of Si and Mg followed by Si–Mg coclustering. This stage is followed by the formation of fine-scale zones or precipitates and progressively β″, β′, and β precipitation. Apart from the β phase, the ratio of Mg and Si in all decomposition products was found to be ~1:1. A subsequent 3DAP study by Murayama and Hono [108] suggests that the atom ratio of Mg and Si in the GP zones and the β″ precipitates varies, depending on the alloy composition such that precipitation of Mg_2Si occurs only in alloys with the Al–Mg_2Si quasibinary composition. These workers also examined the mechanism of natural aging, the evolution of precipitation from the coclusters to β″, and the role of excess Si on the kinetics of the age-hardening response [108].

The natural aging response is higher in the Si excess alloy (Fig. 21), which also has a significantly higher age-hardening response when aged at 175°C [109]. This is undesireable in the context of the automobile body–body sheet fabrication. Figure 22(a) is an HRTEM image of an Al–0.65Mg–0.70Si alloy naturally aged for 70 days. Although no evidence for precipitation is visible in the HRTEM, the 1DAP integrated concentration–depth profile provided in Fig. 22(b) shows evidence of Si–Mg coclustering in the same alloy/condition. Preaging at 70°C increases the density of the precipitate dispersion formed after subsequent aging at 175°C because the GP zones formed during preaging are large enough to serve as heterogeneous nucleation sites for β″ precipitates. On the other hand, the coclusters that form during natural aging (Fig. 22) suppress the hardening response at 175°C because they revert at the artificial aging temperature. The direct observation of solute clusters and GP zones by 3DAP demonstrate convincingly that this mechanism, which is essentially the same as that first proposed by Pashley [104], controls the elevated temperature hardening response.

Effects of Cu Additions

Additions of Cu result in improved tensile properties in 6000 series alloys, and this appears to be mainly due mainly to a refinement in the precipitate dispersion. Recent 3DAP results indicate that Cu is incorporated exclusively in the β″ precipitate phase [110], while Cu is not a constituent of the clusters or GP zones. Although other studies have reported the presence of the Q′ and Q

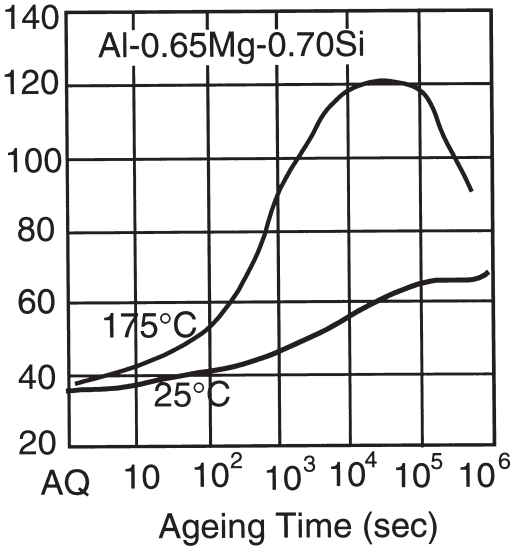

FIG. 21. Hardness–time plots for the Al–Mg–Si alloys aged naturally and at 175°C. After Saga and Kikuchi [109].

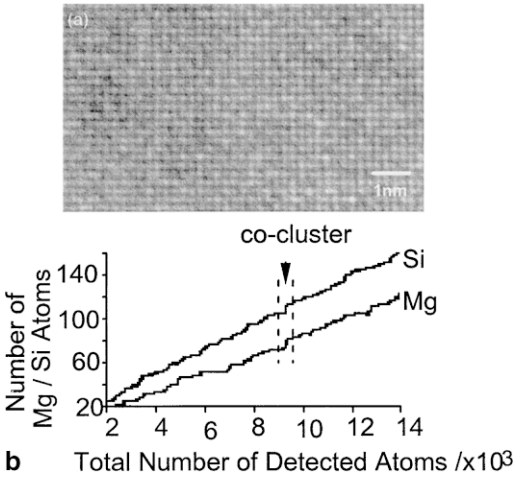

FIG. 22. Analysis of naturally aged Al–0.65Mg–0.70Si alloy. (a) High-resolution transmission electron micorgraphs recorded from the $<001>_\alpha$ orientation; (b) integrated concentration–depth profile (1DAP). After Murayama and Hono [108].

phases ($Al_5Cu_2Mg_8Si_6$) [111], these precipitation products are observed only after prolonged aging at elevated temperatures, and do not appear to contribute to age hardening during the usual industrial heat treatments.

Al–Zn–Mg-BASED ALLOYS

Alloys in the Al–Zn–Mg system (7xxx series) have been widely used as high-strength structural materials. They have a high response to age hardening, as indicated in the hardness–time plots of Fig. 23 [112]. One drawback of these alloys is their susceptibility to stress corrosion cracking (SCC), and this restricts their use in peak hardness conditions. There have been many studies of precipitation hardening in these alloys; however, the small precipitate size makes determination of the crystallographic and chemical characteristics difficult, and some ambiguity remains over these details and the precipitation sequence. Therefore, this system is an example where APFIM and TEM can provide a new insight into the microstructure–property relationship, which is important for rational alloy design. There appears to be a need for further work to clarify details of the complex microstructural evolution in this system.

The following precipitation processes have been identified in Al–Zn–Mg alloys when they are aged at temperatures below the GP zone solvus [113–115]:

$$SSSS \rightarrow \text{GP zones} \rightarrow \eta' \rightarrow \eta$$

There is wide agreement that the GP zones precede the formation of η', which possesses a $\{111\}_\alpha$ habit plane. The equilibrium η phase ($MgZn_2$, C14, a = 0.496nm, c = 1.402nm) is known to occur in up to nine orientations, designated η_1–η_9 [116]. One of these, designated η_2, is oriented such that $(10.0)_{\eta_2}//\{110\}_\alpha$ and $(00.1)_{\eta_2}//\{111\}_\alpha$ exhibit the same precipitate trace as that for η'. Moreover, it has been proposed that the $\eta' \rightarrow \eta$ transformation may be nucleated at the existing η' precipitates, and occurs directly rather than through dissolution and reprecipitation [116–118]. Other work includes a report of a phase designated η'' [119], which precedes the formation of η', although this has not been widely observed.

Despite the importance of GP zones as the first precipitates formed in the decomposition of these alloys, there have been relatively few studies that provide clear data on their shape, structure, and composition, and some debate on these issues remains [113–125]. However, recent 3DAP studies are consistent with the proposal by Mukhopadhyay [125] that GP zones in Al–Zn–Mg alloys form as spherical precipitates, rich in Mg and Zn [122]. Figure 24 is a 3DAP reconstruction showing the distribution of Mg, Zn, and Al atoms in a sample aged 20 h at 90°C [126]. This data suggest that the GP zones contain Mg and Zn in approximately equal concentrations. The observed zone shape and composition seem consistent with the atomic size effects expected from the fact that Zn and Mg are smaller and larger, respectively, than Al, because the negligible net atomic size factor would suggest spherical zones of approximately equal Mg–Zn composition.

Considerable debate remains as to the precise crystallographic structure, orientation, and composition of the η' phase, and these are now reviewed, given the significance of structure on nucleation and growth. Moreover, the structural details are needed to enable an assessment of the potential for strengthening through disloca-

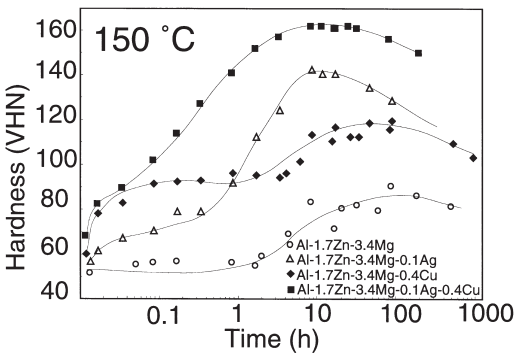

FIG. 23. Hardness–time plots for the Al–1.7Zn–3.4Mg alloy aged at 150°C, showing the effects of individual and combined Ag and Cu additions. After Caraher et al. [112].

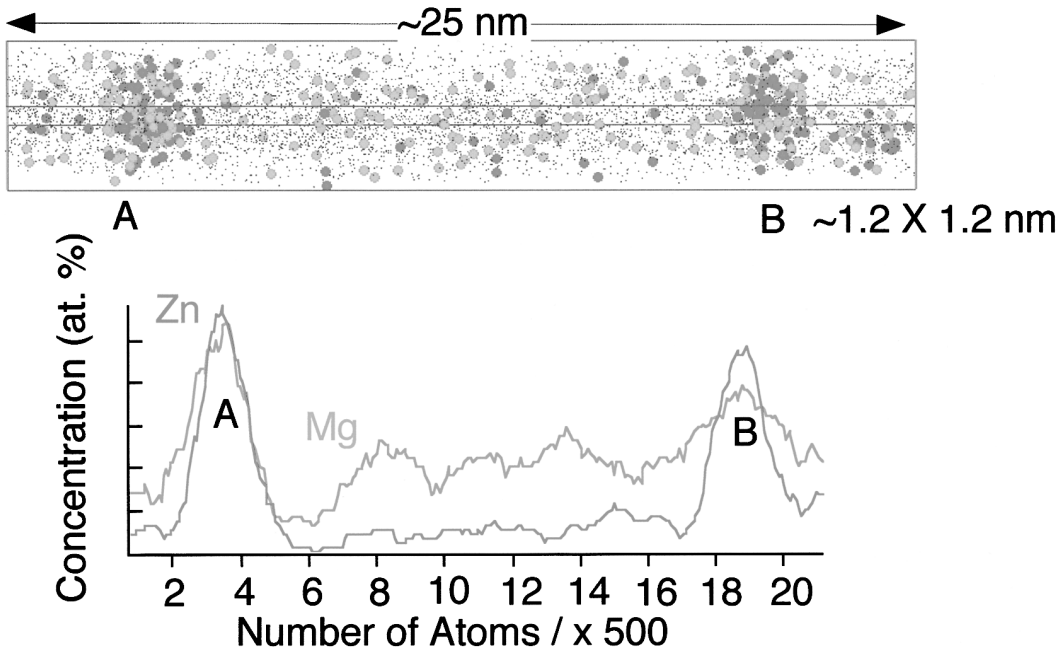

FIG. 24. Three-dimensional reconstruction (3DAP) of the solute distribution in Al–1.7Zn–3.4Mg alloy following ageing at 90°C for 20 h. After Caraher et al. [126].

tion–precipitate interactions. Different hexagonal models for the η′ phase have been proposed [99, 122, 127, 128], together with monoclinic [117] and orthorhombic [129] structural models; however, there is general agreement that the precipitates occur on the matrix $\{111\}_\alpha$ planes. A common feature of all $\{111\}_\alpha$ precipitates observed in the four alloys studied in Fig. 23 was the presence of continuous faceting on $\{111\}_\alpha$ planes when the precipitates were viewed edge-on in $<110>_\alpha$ BF TEM images and low aspect ratio [112]. This observation held for both the finest η′ precipitates as well as coarser η platelets. Figure 25(a) is an example taken from the Al–Zn–Mg–Ag alloy after aging for 2 h at 150°C. The crystallographic form of the η′ phase may be considered in terms of lattice misfit across the precipitate and matrix for the abovementioned structural models. Results are shown in Fig. 25(b)–(c), which includes a sketch of the basic Bravais lattice of the η′ unit cell proposed by Auld and Cousland (P6m2, a = 0.496nm, c = 1.402nm) [128], [Fig. 25(b)] and the correspondence of the η′/α lattices in the $\{110\}_\alpha$ projection [Fig. 25(c)] in which dotted lines represent the proposed unit cell for η′. In Fig. 25(c), the shaded region represents the outline of the experimentally observed crystal form [Fig. 25(a)]. For the structure proposed by Auld and Cousland, the $\{111\}_\alpha$ facets are parallel to $(00.1)_{\eta'}$ and $(\bar{1}2.2)_{\eta'}$. The d-spacings of these planes are 1.402 and 0.2338nm, respectively, which in turn, correspond to $6d_{\{111\}\alpha}$ and $d_{\{111\}\alpha}$ such that there is negligible misfit across these planes. A similar, but slightly higher, misfit in the model proposed by Yan et al. [129]. This is in contrast to the significant misfit that would accumulate across the habit plane for the Gjonnes and Simensen model [116] and the Mondolfo et al. model [120] model, due to the nonparallelism between the $(2\bar{1}0)_{\eta'}$ and $(01.0)_{\eta'}$ planes, respectively, and the $\{111\}_\alpha$ planes. This agreement between the experimental observation of crystal form and the morphology favored on the basis of lattice misfit may be significant given the difficulty in obtaining clear diffraction data uniquely from the η′ phase. Of the available models, only that from Auld and Cousland [128] and Yan et al. [129] exhibit

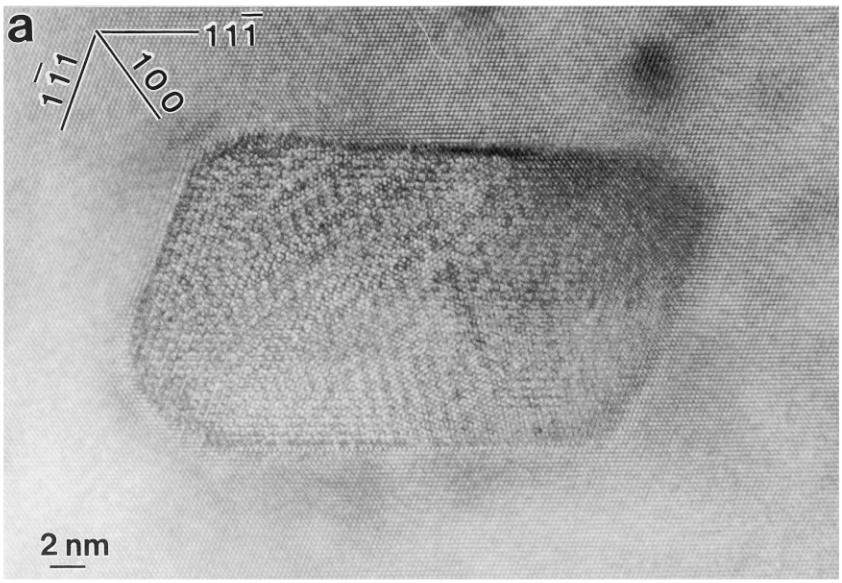

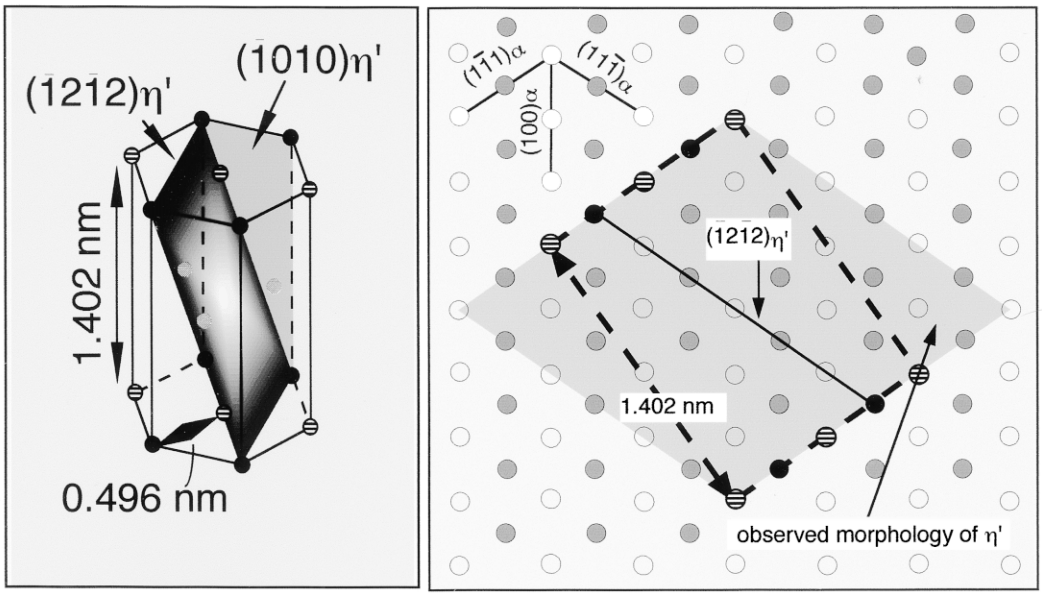

FIG. 25. Analysis of the η′ structure: (a) high-resolution transmission electron micrograph from the Al–1.7Zn–3.4Mg–0.1Ag alloy after aging for 2 h at 150°C; (b) Bravais lattice for the η′ structure as proposed by Auld and Cousland [128], Mondolfo, Gjostein, and Lewinson [120], and Gjonnes and Simensen [116]; (c) correspondence of the η′/α lattices. It may be noted that the $(2110)_{\eta'}$ (c, (ii)) and $(211)_{\eta'}$ (c, (iii)) planes are not parallel to the matrix $\{111\}_{\alpha}$ planes, and that these structures involve significant misfit across the habit precipitate plane. After Caraher et al. [126].

low misfit (<1%) across the $\{111\}_\alpha$ planes, suggesting that these models are more plausible. (It may be noted that the structure proposed by Auld and Cousland [128] and that by Graf [127] differ slightly in the magnitude of the lattice parameters.) This observation may also partially explain the observed precipitate aspect ratio and why there is such limited growth of the η' phase along or across the $\{111\}_\alpha$ facets, because the negligible misfit would provide fewer sites for the nucleation of new ledges and further growth.

There have been a number of studies on the composition of the η' phase [130–136]. Most of these studies have been in quater-

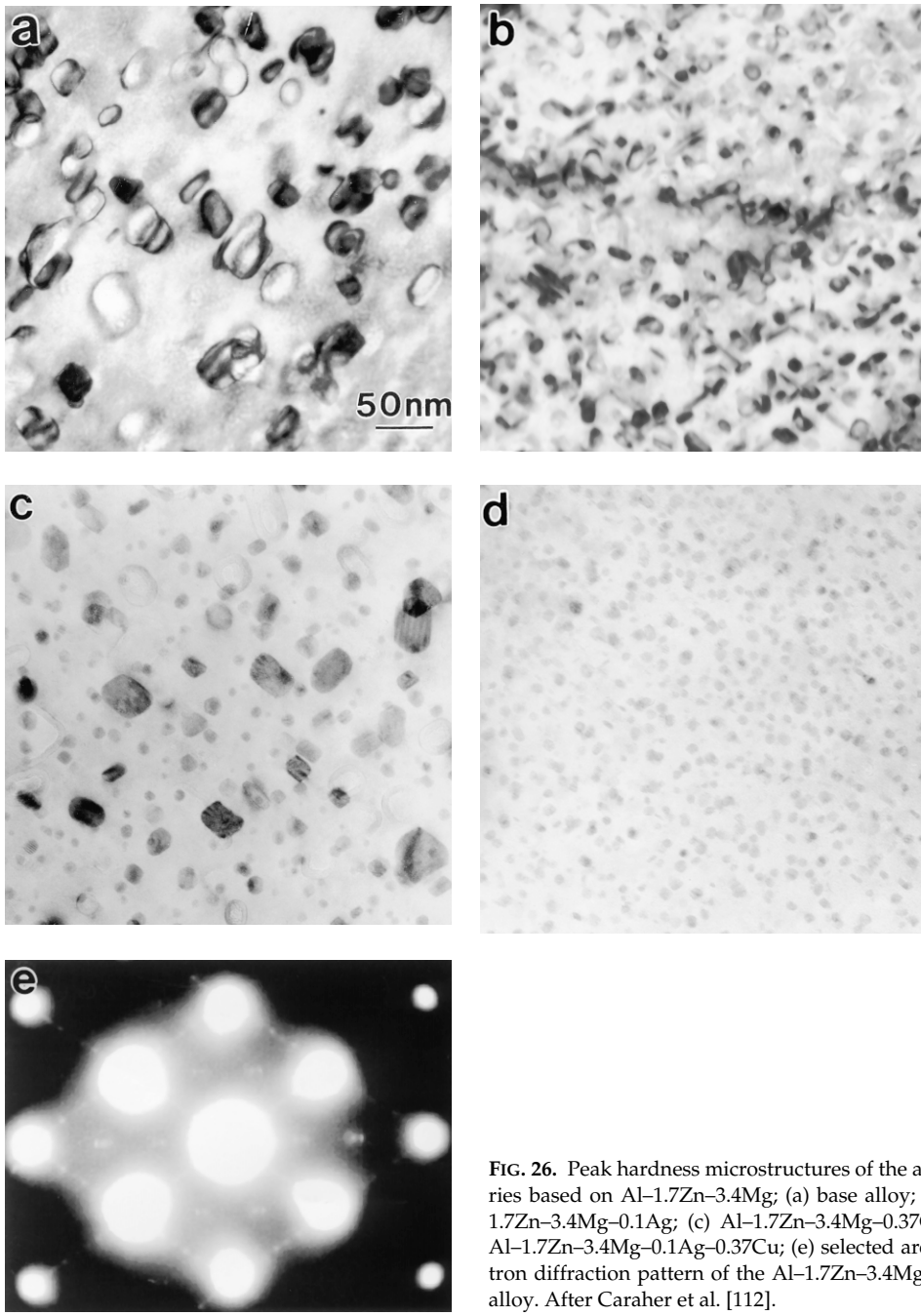

FIG. 26. Peak hardness microstructures of the alloy series based on Al–1.7Zn–3.4Mg; (a) base alloy; (b) Al–1.7Zn–3.4Mg–0.1Ag; (c) Al–1.7Zn–3.4Mg–0.37Cu; (d) Al–1.7Zn–3.4Mg–0.1Ag–0.37Cu; (e) selected area electron diffraction pattern of the Al–1.7Zn–3.4Mg–0.1Ag alloy. After Caraher et al. [112].

nary alloys that contain Cu or Ag. A survey of the results shows that there is some variation in the precipitate compositions reported, although there is general agreement that the phase has a significant Zn deficit from the $MgZn_2$ composition first proposed [120]. The assessment of composition is also complicated by the suggestion that the precipitate chemistry changes during the aging process [118, 126, 134, 135].

Effects of Cu and Ag

It is well known that the addition of Cu (e.g., ~0.5 at. %) is beneficial in both increasing tensile properties and decreasing susceptibility to stress corrosion cracking [84]. Similar effects are also observed in Al–Zn–Mg alloys containing small amounts (e.g., 0.1 at. %) of Ag [136]. For aging in the range of 100–235°C, Cu additions produce a very rapid hardening (Fig. 23), suggesting that a phenomenon distinct from the basic aging processes of the ternary alloys occurs. Despite the rapid hardening effect, Cu additions do not affect the second stage of hardening (Fig. 22) [112–115, 136].

Figure 26(a)–(d) provides $<110>_\alpha$ BF TEM images of the four alloys studied in Fig. 23 in the peak hardness condition [112]. Despite the similarity in lattice parameters of these phases, the presence of reflections at 1/3 and 2/3 $\mathbf{g}\{220\}_\alpha$ is used to identify the η' precipitate, because these reflections are predicted from the above structural models. On this basis, the addition of Ag clearly refines the precipitate dispersion and the diffraction patterns such as that in Fig. 26(e) show clear evidence of the η' precipitate phase together with η_2. Recent 3DAP experiments have shown that Ag is partitioned into the η' phase in this alloy, and that this follows the clustering of Ag with Mg and Zn from the early stages of aging [126]. Because the addition of Ag reduces the PFZ width, it is thought that the quenched-in vacancies are retained from the solution treatment and that this accelerates subsequent diffusion and precipitation kinetics. To date, no clear evidence for the formation of GP zones or other distinct precursor phases has been detected in the microstructure of the alloys included in Fig. 23 following aging at 150°C [112], suggesting that the Ag additions may facilitate the direct nucleation of the η' phase.

Atom-probe data from Cu containing Al–Zn–Mg alloys indicates that Cu is contained within all precipitates formed in these alloys [126, 130–135]. It is apparent from Fig. 26 that the effect of the addition of Cu and/or Ag is to mostly influence the dispersion of the precipitation rather than introduce new metastable precipitates, when aged at 150°C. Recent 3DAP work has not found evidence of distinct precursor phases or clustering of Cu prior to nucleation of η'/η_2 [126]. Given the presence of Cu within the precipitate composition, the mechanism of the rapid hardening in the Cu-containing alloys and the refinement in the precipitate dispersion may be related to a lowering of the solvus of the η'/η_2 and a reduction in the nucleation barrier.

Funding support from the Australian Research Council, the Japan Society for the Promotion of Science, the Science and Technology Agency (Japan), and NEDO International Joint Research Grant are gratefully acknowledged. The authors are indebted to Emeritus Professor I. J. Polmear and Professor B. C. Muddle for many stimulating discussions and ideas. Discussions and assistance in the preparation of the manuscript from Ms. Sally Caraher (Monash University), Mr. C. R. Hutchinson (The University of Virginia), Dr. Mitsuhiro Murayama, and Mr. Lajos Reich (NRIM) are gratefully appreciated.

References

1. I. J. Polmear: Control of precipitation processes and properties in aged aluminium alloys by trace element additions. *Proc. 6th Intl Conf on Aluminium Alloys,* ICAA6, Toyohashi, Japan, July 5–10, 1998, eds. T. Sato, S. Kumai, T. Kobayshi and Y. Murakami, The Japan Inst. of Light Metals, 1998, Tokyo, Japan, pp. 75–86.
2. A. K. Mukhopadhyay, G. J. Shiflet, and E. A. Starke: The role of trace alloy additions on precipitation in age hardenable aluminium alloys. In *Morris E. Fine Symposium*, P. K. Liaw, J. R. Weert-

man, H. L. Marcus, and J. S. Santner, eds., TMS, Warrendale, PA, pp. 283–293 (1991).

3. M. K. Miller and G. D. W. Smith: *Atom Probe Microanalysis-Principles and Applications to Materials Problems*, Materials Research Society, Pittsburgh, p. 46 (1989).
4. P. B. Hirsch, A. Howie, R. B. Nicholson, D. W. Pashley, and M. J. Whelan: *Electron Microscopy of Thin Crystals*, Krieger, NY (1977).
5. K. Hono, T. Hashizume, and T. Sakurai: The IMR atom probe. *Surface Sci.* 266:506–512 (1992).
6. K. Hono, R. Okano, T. Saeda, and T. Sakurai: The performance of the IMR three-dimensional atom probe. *Appl. Surface Sci.* 87/88:453–457 (1995).
7. D. Blavette, B. Deconihout, A. Bostel, J. M. Sarrou, M. Bouet, and A. Menand: The tomographic atom probe: A quantitative three-dimensional nanoanalytical instrument on an atomic scale. *Rev. Sci. Instrum.* 64:2911–2919 (1993).
8. E. D. Boyes and F. L. Gai: Proc. *EMAG 75*, Academic Press, NY, p. 267 (1976).
9. T. Abe, K. Miyazaki, and K. Hirano: Imaging of pure Al and aged Al-4wt. % Cu alloys by field ion microscopy. *Acta Metall.* 30:357–366 (1982).
10. M. Wada, H. Kita, and T. Mori: FIM observation of GP zones in an Al–4Cu alloy. *Acta Metall.* 33: 1631–1635 (1985).
11. K. Hono, T. Satoh, and K. Hirano: Evidence of multi-layer GP zones in Al-1.7 at. % Cu alloy. *Philos. Mag.* 53A:495–504 (1986).
12. R. J. Rioja and D. E. Laughlin: The early stages of GP zone formation in naturally aged Al-4wt. % Cu alloys. *Metall. Trans.* 8A:1257–1261 (1977).
13. G. W. Lorimer: Precipitation in aluminium alloys. *Proc. Precipitation Processes in Solids*, K. C. Russell and H. I. Aaronson, eds., TMS-AIME, Warrendale, PA, pp 87–120 (1978).
14. R. B. Nicholson, G. Thomas, and J. Nutting: Electron microscopic studies of precipitation in aluminium alloys. *J. Inst. Met.* 87:429–438 (1958–59).
15. H. K. Hardy: Ageing curves at 110°C on binary and ternary Al–Cu alloys. *J. Inst. Met.* 82:236–238 (1953–54).
16. H. K. Hardy: The ageing characteristics of ternary aluminium–copper alloys with cadmium, indium or tin. *J. Inst. Met.* 80:483–492 (1951–52).
17. J. M. Silcock, T. J. Heal, and H. K. Hardy: Structural ageing characteristics of binary aluminium–copper alloys. *J. Inst. Met.* 82:239–248 (1953–54).
18. V. A. Phillips: Lattice resolution measurement of strain fields at Guinier-Preston zones in Al-3%Cu. *Acta Metall.* 21:219–228 (1973).
19. V. A. Phillips: High resolution electron microscope observations on precipitation in Al-3%Cu alloy. *Acta Metall.* 23:751–767 (1973).
20. R. H. Beton and E. C. Rollason: Hardness reversion of dilute aluminium copper and aluminium copper magnesium alloys. *J. Inst. Met.* 86:77–85 (1957–58).
21. J. L. Murray: The Al–Cu system. *Int. Met. Rev.* 30: 211–233 (1985).
22. K. Osamura, Y. Murakami, T. Sato, T. Takahashi, T. Abe, and K. Hirano: Structure of GP zones in an Al-1.7 at. % Cu alloy aged for 14 years at room temperature. *Acta Metall.* 31:1669–1673 (1983).
23. T. Federighi: Quenched-in vacancies and rate of formation in aluminium alloys. *Acta Metall.* 6: 379–389 (1958).
24. W. DeSorbo, H. N. Treaftis, and D. Turnbull: Rate of clustering in Al–Cu alloys at low temperatures. *Acta Metall.* 6:401–413 (1958).
25. E. Matsubara and J. B. Cohen: Local atomic arrangements in the solid solution of Al-1.7 at. % Cu at 793K. *Acta Metall.* 31:2129–2135 (1983).
26. A. Guinier: Structure of age hardenable Al–Cu alloys. *Nature* 142:569 (1938).
27. G. D. Preston: *Nature* 142:570 (1938).
28. H. Yoshida, H. Hashimoto, Y. Yokota, and N. Ajika: High resolution lattice images of GP zones in an Al-3.97 wt. % Cu alloy. *Trans. Jpn. Inst. Met.* 24:378–385 (1983).
29. M. Karlik and B. Jouffrey: High resolution electron microscopy of Guinier-Preston (GP1) zones in Al–Cu based alloys. *Acta Mater.* 45:3251–3263 (1997).
30. P. S. Rudman and B. L. Averbach: X-ray measurements of local atomic arrangements in aluminium–zinc and in aluminium–silver solid solutions. *Acta Metall.* 2:576–582 (1954).
31. A. Bigot: PhD thesis, The University of Rouen, France (1998).
32. J. W. Cahn and G. Kalonji: Symmetry in solid state transformations morphologies. In *Proc. Intl. Conf. on Solid-Solid Phase Transformations*, Carnegie-Mellon University, Pittsburgh, PA, Aug. 10–14, 1981, H. I. Aaronsson, D. E. Laughlin, R. F. Sekerka, and C. M. Wayman, eds., The Metall. Soc. of the AIME, Pittsburgh, PA, pp. 3–14 (1981).
33. F. C. Phillips: *An Introduction to Crystallography*, Longmans, New York (1960).
34. A. J. Bradley and P. Jones: An X-ray investigation of the Cu–Al alloys. *J. Inst. Met.* 51:131–162 (1933).
35. D. Vaughan and J. M. Silcock: The orientataion and shape of θ precipitates formed in an Al–Cu alloy. *Phys. Stat. Sol.* 20:725–736 (1967).
36. A. H. Sully, H. K. Hardy, and T. J. Heal: The aluminium-tin phase diagram and the characteristics of aluminium alloys containing tin as an alloying element. *J. Inst. Met.* 76:269–294 (1949–50).
37. J. M. Silcock, T. J. Heal, and H. K. Hardy: The structural ageing characteristics of ternary aluminium–copper alloys with cadmium, indium or tin. *J. Inst. Met.* 84:23–31 (1955).

38. I. J. Polmear and H. K. Hardy: Some metallographic observations on aged aluminium–copper alloys. *J. Inst. Met.* 81:427–432 (1952–53).
39. J. D. Boyd and R. B. Nicholson: A calorimetric determination of precipitate interfacial energies in two Al–Cu alloys. *Acta Metall.* 19:1101–1109 (1971).
40. R. Sankaren and C. Laird: Effects of trace additions Cd, In and Sn on the interfacial structure and kinetics of growth of θ′ plates in Al–Cu alloy. *Acta Metall.* 22:957–969 (1974).
41. H. Suzuki, M. Kanno, and I. Araki: Precipitation of the intermediate phase in Al–Cu–Sn alloys. *J. Jpn. Inst. Light Met.* 25:413–421 (1975).
42. M. Kanno, H. Suzuki, and O. Kanoh: *J. Jpn. Inst. Light Met.* 29:223–226 (1979).
43. M. Kanno, H. Suzuki, and O. Kanoh: The precipitation of θ′ phase in an Al–4Cu–0.06In alloy. *J. Jpn. Inst. Met.* 44:1139–1145 (1980).
44. J. B. M. Van Nuyten: Quenched structures and precipitation in Al–Cu alloys with and without trace additions of Cd. *Acta Metall.* 15:1765–1770 (1967).
45. S. P. Ringer, K. Hono, and T. Sakurai: The effect of trace additions of Sn on precipitation in Al–Cu alloys: An atom probe field ion microscopy study. *Metall. Mater. Trans.* 26A:2207–2217 (1995).
46. A. H. Geisler: *Phase Transformations in Solids*, Wiley, New York, p. 387 (1951).
47. P. C. Varley, K. B. Day, and A. Sendorek: The structure and mechanical properties of high purity Al–Zn–Mg alloys. *J. Inst. Met.* 86:337–350 (1957–58).
48. J. L. Taylor: The effect of heat treatment on the grain boundary zones in a high purity Al–Zn–Mg alloy. *J. Inst. Met.* 92:301–302 (1963–64).
49. J. D. Embury and R. B. Nicholson: The nucleation of precipitates: The system Al–Zn–Mg. *Acta Metall.* 13:403–417 (1965).
50. G. B. Brook: *Precipitation in Metals*, Spec. Rep. No. 3, Fulmer Res. Inst., UK (1963).
51. I. J. Polmear and R. J. Chester: Abnormal age hardening in an Al–Cu–Mg alloy containing silver and lithium. *Scripta Metall.* 23:1213–1217 (1989).
52. I. J. Polmear and M. Couper: Design and development of an experimental wrought aluminium alloy for use at elevated temperatures. *Metall. Trans.* 19A:1027–1035 (1988).
53. J. R. Pickens, F. H. Heubaum, T. J. Langan, and L. S. Kramer: Al–Cu–Li–Mg–Ag–Zr Alloy Weldalite™ 049. In *Proc. 5th* Conf. Al–Li Alloys, Williamsburg, VA, March 1989, Materials and Component Engineering Publications Ltd., Birmingham, UK, p. 1397 (1989).
54. S. P. Ringer, K. Hono, I. J. Polmear, and T. Sakurai: Nucleation of precipitates in aged Al–Cu–Mg–(Ag) alloys with high Cu:Mg ratios. *Acta Mater.* 44:1883–1898 (1996).
55. J. M. Silcock: The structural ageing characteristics of Al–Cu–Mg alloys with copper:magnesium weight ratios of 7:1 and 2.2:1. *J. Inst. Met.* 89:203–210 (1960–61).
56. Yu. A. Bagaryatsky: *Doklady Akad. Nauk SSSR* 87: 559–562 (1952).
57. H. Perlitz and A. Westgren: The crystal structure of Al_2CuMg. *Arkiv. Kemi. Mineral. Geol.* 16B (1943).
58. J. A. Taylor, B. A. Parker, and I. J. Polmear: Precipitation in Al–Cu–Mg–Ag casting alloy. *Met. Sci.* 12:478–482 (1978).
59. R. J. Chester and I. J. Polmear: Precipitation in Al–Cu–Mg–Ag alloys. In *The Metallurgy of Light Alloys*, Inst. of Metals, London, pp. 75–81 (1983).
60. K. M. Knowles and W. M. Stobbs: The structure of {111} age-hardening precipitates in Al–Cu–Mg–Ag alloys. *Acta Crystallogr.* B44:207–227 (1988).
61. B. C. Muddle and I. J. Polmear: The precipitate Ω phase in Al–Cu–Mg–Ag alloys. *Acta Metall.* 37: 777–789 (1989).
62. A. Garg and J. M. Howe: Convergent beam electron diffraction analysis of the Ω phase in an Al–Cu–Mg–Ag alloy. *Acta Metall. Mater.* 39:1939–1946 (1991).
63. Y. C. Chang: Ph.D. thesis, Crystal structure and nucleation behaviour of {111} precipitates in an Al–3.9Cu–0.5Mg–0.5Ag (wt. %) alloy. Carnegie Mellon University (1992).
64. Y. C. Chang and J. M. Howe: Composition and stability of Ω phase in an Al–Cu–Mg–Ag alloy. *Metall Trans.* 24A:1461–1470 (1993).
65. K. Hono, N. Sano, S. S. Babu, R. Okano, and T. Sakurai: Atom probe study of the precipitation process in Al–Cu–Mg–Ag alloys. *Acta Metall. Mater.* 41:829–838 (1993).
66. A. Garg, Y. C. Chang, and J. M. Howe: Precipitation of the Ω phase in an Al–4Cu–0.5Mg alloy. *Scripta Metall.* 24:677–680 (1990).
67. R. W. Fonda, W. A. Cassada, and G. J. Shiflet: Accommodation of the misfit strain surrounding {111} precipitates (Ω) in Al–Cu–Mg–(Ag). *Acta Metall. Mater.* 40:2539–2546 (1992).
68. J. M. Howe: Analytical transmission electron microscopy analysis of Ag and Mg segregation to {111} θ precipitate plates in an Al–Cu–Mg–Ag alloy. *Philos. Mag. Lett.* 70:111–121 (1994).
69. S. P. Ringer, W. Yeung, B. C. Muddle, and I. J. Polmear: Precipitate stability in Al–Cu–Mg–Ag alloys aged at high temperatures. *Acta Metall. Mater.* 42:1715–1725 (1994).
70. K. Hono, T. Sakurai, and I. J. Pomear: Pre-precipitate clustering in an Al–Cu–Mg–Ag alloy. *Scripta Metall. Mater.* 30:695–700 (1994).
71. M. Murayama and K. Hono: Three dimensional

atom probe analysis of pre-precipitate clustering in an Al–Cu–Mg–Ag alloy. *Scripta Mater.* 38: 1315–1319 (1998).

72. L. Reich, M. Murayama, and K. Hono: Evolution of Ω phase in an Al–Cu–Mg–Ag alloy—A three dimensional atom probe study. *Acta Mater.* 46: 6053–6062 (1998).
73. I. S. Suh and J. K. Park: Influence of the elastic strain energy on the nucleation of Ω phase in Al–Cu–Mg–(Ag) alloys. *Scripta Mater.* 33:205–211 (1995).
74. Q. Cui, G. Itoh, and M. Kanno: Effect of silver addition on the precipitation of the Ω phase in an Al–Cu–Mg–Ag alloy. *J. Jpn. Inst. Met.* 59:492–498 (1995).
75. G. Itoh, Q. Cui, and M. Kanno: Effects of a small addition of magnesium and silver on the precipitation of T1 phase in an Al–4Cu–1.1Li–0.2Zr (wt. %) alloy. *Mater. Sci. Eng.* A211:128–137 (1996).
76. W. A. Cassada, G. J. Shiflet, and E. A. Starke, Jr.: The effect of plastic deformation on Al_2CuLi (T_1) precipitation. *Metall. Trans. A* 22A:299–306 (1991).
77. J. M. Howe, J. Lee, and A. K. Vasudevan: Structure and deformation behaviour of T_1 precipitate plates in an Al–2Li–1Cu alloy. *Metall. Trans.* 19A: 2911–2926 (1988).
78. R. A. Herring, F. W. Gayle, and J. R. Pickens: High resolution electron microscopy study of a high copper variant of weldalite 049 and a high strength Al–Cu–Ag–Mg–Zr alloy. *J. Mater. Sci.* 28:69–73 (1993).
79. Y.-S. Lee, S. P. Ringer, I. J. Polmear, and B. C. Muddle: Precipitate stability in alloys based on the Al–Cu system. In *4th Intl. Conf. on Aluminium Alloys—Their Physical and Mechanical Properties (ICAA4)*, T. H. Sanders, Jr. and E. A. Starke, Jr., eds., Georgia Institute of Technology, Atlanta, GA, September 11–16, pp. 582–589 (1994).
80. Y.-S. Lee, B. C. Muddle, and I. J. Polmear: High strength Al–Cu–Mg–Ag alloys with controlled Li additions. In *Proc. 2nd Pacific Rim Intl. Conf. on Advanced Materials and Processing*, K. S. Kim, J. K. Moon, and S. J. Kim, eds., Korean Inst. of Metals and Materials, Kyongju (1995).
81. B.-P. Huang and Z.-Q. Wang: Effects of Li content on precipitation in Al–Cu–(Li)–Mg–Ag–Zr alloys. *Scripta Mater.* 38:357–362 (1998).
82. S. P. Ringer, K. Hono, I. J. Polmear, and T. Sakurai: Atom probe study of the effects of Ag and Mg additions on precipitation processes in Al–Cu and Al–Cu–Li alloys. In *Intl. Conf. on Solid-Solid Phase Transformations in Inorganic Materials*, Pittsburgh, PA, July 17–22, W. C. Johnson, J. M. Howe, D. E. Laughlin, and W. A. Soffa, eds., TMS, Warrendale, PA, pp. 165–170 (1994).
83. L. Reich, M. Murayama, and K. Hono: 3DAP study of the effect of Mg and Ag additions on precipitation in Al–Cu–(Li) alloys. In *Proc. 6th* International Conference on Aluminium Alloys (ICAA6), July 5–10, 1998, T. Sato, S. Kumai, T. Kobayashi, and Y. Murakami, eds., Toyohashi, Japan, Japan Institute for Light Metals, Tokyo, vol. 2, pp. 739–744 (1998).
84. I. J. Polmear: Light alloys: Metallurgy of the light metals. Arnold, London 3rd ed. (1995).
85. J. T. Vietz and I. J. Polmear: The influence of small additions of silver on the ageing of aluminium alloys: Observations on Al–Cu–Mg alloys. *J. Inst. Met.* 94:410–419 (1966).
86. S. P. Ringer, K. Hono, T. Sakurai, and I. J. Polmear: Cluster hardening in Al–Cu–Mg alloys. *Scripta Mater.* 36:517–521 (1997).
87. S. P. Ringer, T. Sakurai, and I. J. Polmear: On the origins of hardening in Al–Cu–Mg–(Ag) alloys. *Acta Mater.* 45:3731–3744 (1997).
88. L. Reich, S. P. Ringer, and K. Hono: *Philos. Mag. Lett.* (in press).
89. R. B. Nicholson: The interaction between point defects and solute atoms in aluminium alloys. In *Intl. Conf. on Electron Diffraction and the Nature of Defects in Crystals*, August 16–21, 1965, Australian Academy of Science, Intl. Union of Crystallog. and Intl. Union of Pure and Appl. Phys., Australian Acad. Sci., Melbourne, II N-2 (1965).
90. P. Ratchev, B. Verlinden, P. De Smet, and P. Van Houtte: Precipitation hardening of an Al-4.2 wt. % Mg 0.6 wt. % Cu alloy. *Acta Mater.* 46:3523–3533 (1998).
91. J. T. Staley: Metallurgical aspects affecting strength of heat treatable alloy products used in the aerospace industry. In *Proc. 3rd Intl. Conf: Aluminium Alloys—Their Physical and Mechanical Properties (ICAA3)*, June 22–26, 1992, L. Arnberg, O. Lohne, E. Nes, and N Ryum, eds., Norwegian Institute Of Technology, Trondheim, Norway, vol. 3, pp. 107–129 (1992).
92. S. P. Ringer, S. K. Caraher, and I. J. Polmear: Response to comments on cluster hardening by Zahra et al. *Scripta Mater.* 39:1559–1567 (1998).
93. A. M. Zahra, C. Y. Zahra, C. Alfonso, and A. Charai: Comments on cluster hardening in an aged Al–Cu–Mg alloy. *Scripta Mater.* 39:1553–1558 (1998).
94. S. P. Ringer, K. Hono, I. J. Polmear, and T. Sakurai: Precipitation processes during the early stages of aging in Al–Cu–Mg alloys. *Appl. Surface Sci.* 94/95:253–260 (1996).
95. R. N. Wilson and P. G. Partridge: The nucleation and growth of S′ precipitates in an aluminium–2.5%copper–1.2%magnesium alloy. *Acta Metall.* 13:1321–1327 (1965).
96. A. K. Gupta, P. Gaunt, and M. C. Chaturvedi: The crystallography and morphology of the S′-phase in an Al(CuMg) alloy. *Philos. Mag.* A55: 375–387 (1987).
97. J. K. Park and A. J. Ardell: Microstructures of the commercial 7075 Al alloy in the T651 and T& tempers. *Metall Trans.* 14A:1957–1965 (1983).

98. H. D. Chopra, K. J. Liu, B. C. Muddle, and I. J. Polmear: The structure of metastable $\{111\}_\alpha$ precipitates in an Al-2.5wt. % Cu-1.5 wt. % Mg −0.5 wt. % Ag alloy. *Philos. Mag. Lett.* 71:319–325 (1995).
99. J. H. Auld, J. T. Vietz, and I. J. Polmear: T phase precipitation induced by addition of silver to an Al–Cu–Mg alloy. *Nature* 209:703–704 (1966).
100. G. Bergman, J. L. T. Waugh, and L. Pauling: The crystal structure of the metallic phase $Mg_{32}(AlZn)_{49}$. *Acta Crystallog.* 10:254 (1952).
101. S. P. Ringer, G. C. Quan, and T. Sakurai: Microstructural evolution in high strength microalloyed aluminium alloys. *J. Mater. Sci. Eng.* 250A: 120–125 (1998).
102. H. D. Chopra, B. C. Muddle, and I. J. Polmear: The structure or primary strengthening precipitates in an Al-1.5 wt. % Cu-4.0 wt. % Mg-0.5 wt. % Ag alloy. *Philos. Mag. Lett.* 73:351–357 (1996).
103. G. Thomas: The aging characteristics of aluminium alloys: Electron transmission studies of Al–Mg–Si alloys. *J. Inst. Met.* 90:57–62 (1961)
104. D. W. Pashley, M. H. Jacobs, and J. T. Vietz: *Philos. Mag.* 16A:51–76 (1967).
105. I. Dutta and S. M. Allen: Calorimetric study of precipitation in commercial Al alloys. *J. Mater. Sci. Lett.* 10:323–326 (1991).
106. S. Ceresara, E. D. Russo, P. Fiorini, and A. Giarda: *Mater. Sci. Eng.* 5:220–227 (1969/70).
107. G. A. Edwards, K. Stiller, G. L. Dunlop, and M. J. Couper: The precipitation sequence in Al–Mg–Si alloys. *Acta Mater.* 46:3893–3904 (1998).
108. M. Murayama and K. Hono: Pre-precipitate clusters and precipitation processes in Al–Mg–Si alloys. *Acta Mater.* 47:1537–1548 (1998).
109. M. Saga and M. Kikuchi: Unpublished research, Nippon Steel Corporation (1998).
110. M. Murayama and K. Hono: Distribution of Cu atoms during aging of Al–Mg–Si–Cu alloy. *Proc. 6th Intl. Conf. on Al Alloys* (ICAA6), Toyohashi, Japan, July 5–10, 1998, eds. T. Sato, S. Kumai, T. Kobayashi and Y. Munakami, The Japan Inst. of Light Metals, 1998, Tokyo, Japan, pp. 837–842.
111. A. K. Gupta, P. H. Marois, and D. J. Lloyd. *Mater. Sci. For.* 217–222:801–808 (1996).
112. S. K. Caraher, I. J. Polmear, and S. P. Ringer: Effects of Cu and Ag on precipitation in Al–4Zn–3Mg (wt. %). In *Proc. 6th Intl. Conf. Aluminium Alloys (ICAA6)*, July 5–10, 1998, T. Sato, S. Kumai, T. Kobayashi, and Y. Murakami, eds. Toyohashi, Japan, Japan Institute for Light Metals, Tokyo, Vol. 2, pp. 739–744, (1998).
113. I. J. Polmear: The ageing characteristics of ternary aluminium–zinc–magnesium alloys. *J. Inst. Met.* 86:113–121 (1957–58).
114. I. J. Polmear: The upper temperature limit of stability of GP zones in ternary aluminium–zinc–magnesium alloys. *J. Inst. Met.* 87:24–25 (1958–59).
115. J. T. Vietz, K. R. Sargant, and I. J. Polmear: The influence of small additions of silver on the ageing of aluminium alloys: Further observations on Al–Zn–Mg alloys. *J. Inst. Met.* 92:327–333 (1963–64).
116. J. Gjønnes and C. J. Simensen: An electron microscope investigation of the microstructure in an aluminium–zinc–magnesium alloy. *Acta Metall.* 18:881–890 (1970).
117. H. Y. Hunsicker: Development of Al–Zn–Mg–Cu alloys for aircraft. In *Proc. Rosenhain Centenary Conf. on the Contribution of Physical Metallurgy to Engineering Practice*, Royal Society of London, London, pp. 359–376 (1976).
118. A. Yamamoto, K. Minami, U. Ishihara, and H. Tsubakino: Calorimetric and resistivity study on the formation and redissolution of precipitates in 7050 aluminium alloy. *Mater. Trans. JIM* 39:69–74 (1998).
119. P. A. Thackery: The nature and morphology of precipitates in Al–Zn–Mg alloys. *J. Inst. Met.* 96: 228–235 (1968).
120. L. F. Mondolfo, N. A. Gjostein, and D. W. Lewinson: Structural changes during the ageing of an Al–Mg–Zn alloy. *Trans. AIME* 206:1378–1385 (1956).
121. G. Thomas and J. Nutting: The ageing characteristics of aluminium alloys, electron microscope studies of alloys based on the aluminium zinc magnesium system. *J. Inst. Met.* 88:81–90 (1959–60).
122. H. Schmalzried and V. Gerold: Rontgenographische untersuchungen uberdie ausartung einer aluminium-magnesium-zink-legierung. *Z. Metallkund.* 49:291–301 (1957).
123. R. W. Gould and V. Gerold: The influence of Mg atoms on diffusion processes in Al–Zn alloys. *Acta Metall.* 12:954–955 (1964).
124. S. R. Ortner, C. R. M. Grovenor, and B. A. Sholock: On the structure and composition of GP zones in high purity Al–Zn–Mg alloys. *Scripta Metall.* 22:843–846 (1988).
125. A. K. Mukhopadhyay: Guinier-Preston zones in a high purity Al–Zn–Mg alloy. *Philos. Mag. Lett.* 70: 135–140 (1994).
126. S. K. Caraher, K. Hono, I. J. Polmear, and S. P. Ringer: unpublished research.
127. R. Graf: The ageing of ternary aluminium–zinc–magnesium alloys. *J. Inst. Met.* 86:535–536 (1956).
128. J. H. Auld and S. Mck. Cousland: The structure of the metastable η′ phase in aluminium–zinc–magnesium alloys. *J. Aust. Inst. Met.* 19:194–201 (1974).
129. J. Yan, L. Chunzhi, and Y. Minggao: On the crystal structure of S′ phase in Al-Cu-Mg alloy. *Mater. Sci. Eng.* A141:123–128 (1991).
130. S. R. Ortner and C. R. M. Grovenor: Atom probe analysis of precipitates in AlZnMg alloy 7018. *Scripta Mater.* 22:839–842 (1988).
131. S. S. Brenner, J. Kowalik, and M. J. Hua: FIM/

atom probe analysis of a heat treated 7150 aluminium alloy. *Surface Sci.* 246:210–217 (1991).

132. P. J. Warren, C. R. M. Grovenor, and J. S. Cromton: *Surface Sci.* 266:342 (1992).
133. K. Hono, N. Sano, and T. Sakurai: Quantitative atom probe analysis of some aluminium alloys. *Surface Sci.* 266:350–357 (1992).
134. A. Bigot, F. Danoix, P. Auger, D. Blavette, and A. Reeves: Tomographic atom probe study of age hardening precipitation in industrial AlZnMgCu (7050) alloy. *Mater. Sci. For.* 217–222:695–700 (1996).
135. K. Stiller, V. Hansen, M. Knutson-Wedel, G. Waterloo, and J. Gjonnes: Hardening precipitates and their precursors in 7XXX alloys. In *Proc. 6th* Intl. Conf. Aluminium Alloys (ICAA6), July 5–10, 1998, T. Sato, S. Kumai, T. Kobayashi, and Y. Murakami, eds. Toyohashi, Japan, Japan Institute for Light Metals, Tokyo, vol. 2, pp. 615–620 (1998).
136. I. J. Polmear: The ageing characteristics of complex Al–Zn–Mg alloys: Distinctive effects of Cu and Ag on the ageing mechansim. *J. Inst. Met.* 89: 51–59 (1960).

Received November 1998; accepted December 1998.